CRYSTAL GROWTH & DESIGN

pubs.acs.org/crystal

Article

Conformational and Nonconformational Polymorphism in 4′-Hydroxyvalerophenone: A Structure−Energetics−Dynamics Perspective

Published as part of a Crystal Growth and Design virtual special issue Remembering the Contributions and Life of Prof. Joel Bernstein

Ricardo G. Simões, Cátia S. D. Lopes, M. Fátima M. Piedade, Carlos E. S. Bernardes, Hermínio P. Diogo, and Manuel E. Minas da Piedade*

Cite This: *Cryst. Growth Des.* 2020, 20, 2321−2336

Read Online

ACCESS | Metrics & More | Article Recommendations | Supporting Information

ABSTRACT: Compounds based on the $HOC_6H_4C(O)R$ (R = H, alkyl, OH, etc.) framework have provided excellent models to investigate the complex interplay of structural and energetic effects behind polymorphism and crystallization as a whole. In this work, the polymorphic behavior of 4′-hydroxyvalerophenone (HVP, R = C_4H_9) was experimentally and theoretically explored from a holistic structural−energetics−dynamics perspective. The molecular and crystal structures of two new forms (II and III) were determined by single crystal X-ray diffraction. They share with the previously known form I, and with analogous systems (R = H, CH_3) that do not contain a flexible R group, an infinite $C_1^1(8)$ chain sustained by "head-to-tail" OH···O═C hydrogen bonds as the main one-dimensional (1D) packing motif. The molecular organization within the chain ("herringbone" type in form I and planar in forms II and III) and the relative orientation of the CO and OH groups (*Z* in form I and *E* in forms II and III) are, however, different. These differences are reflected by the thermodynamic and kinetic relationships between the three polymorphs. Differential scanning calorimetry and microscopy experiments revealed that (i) the structurally very similar III/II pair is enantiotropically related by a fast and reversible phase transition at 247.5 ± 0.4 K. (ii) In contrast, the form II → form I transition is severely hindered, and, although form II is monotropic relative to form I, it can be observed to melt upon heating, or stored for days at ambient pressure and temperature without signs of transformation to form I, unless subjected to a perturbation (e.g., scratching, grinding). These findings are consistent with microscopy and molecular dynamics (MD) simulation results, suggesting that the III → II transition occurs by a concerted displacement of the molecules in the crystal lattice, while the II → I process is compatible with a diffusive nucleation and growth mechanism. It was also found that, despite being metastable, form II preferentially crystallizes from the melt in accordance with Ostwald's rule of stages. MD simulations indicated that this observation is most likely originated by the fact that the structure of liquid HVP is much closer to form II than to form I. Finally, a thermodynamic analysis suggested that the relative stability of the three HVP polymorphs, at 298 K, ranked in terms of Gibbs energy (I > II > III) does not follow the corresponding lattice enthalpy trend (I > III > II). This stresses the importance of accounting for entropy contributions when discussing polymorph stability.

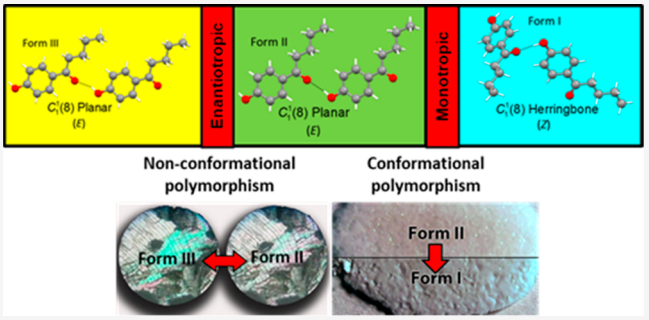

INTRODUCTION

Polymorphism, the existence of different crystalline forms originated from the same molecule, is a commonly observed phenomenon in organic compounds.[1−4] As a quick literature search can show, the considerable interest in this area, already emphasized in Joel Bernstein's seminal book,[1] is still very alive and growing.[5] This interest has been fostered by two main driving forces: First, the control of polymorphism represents a major problem for chemical sectors, such as dyes, agrochemicals, or pharmaceuticals, that rely on the manufacture of products with highly reproducible properties.[1−4] Second, polymorphism control requires a reasonable understanding of the complex interplay of structural, thermodynamic, and kinetic factors behind crystallization[1,6,7] and polymorphic transformations.[8−10]

Received: November 4, 2019
Revised: February 27, 2020
Published: March 2, 2020

https://dx.doi.org/10.1021/acs.cgd.9b01481
Cryst. Growth Des. 2020, 20, 2321−2336

This aspect is still poorly understood at the molecular scale and, as such, constitutes also a challenge for fundamental science.[6,8−10]

Polymorphism is difficult to control because the intermolecular interactions sustaining a crystal structure are typically 1 order of magnitude (or more) weaker than the covalent bonds responsible for the integrity of a molecule. Various packing arrangements with very similar Gibbs energies are, therefore, often accessible to a molecule in a crystallization process. Although the structural unit remains the same, the packing differences are frequently accompanied by changes in physicochemical properties (e.g., color, hardness, melting point, solubility, chemical reactivity), so that different polymorphs are, in fact, different materials. Consequently, as exemplified by various incidents in the pharmaceutical industry (e.g., the Zantac, Ritonavir, and Avalide cases),[1,11] the lack of control over the selective crystallization of specific polymorphs can have serious consequences in terms of manufacture, patenting, and safe use of marketable products.[1] An additional complication is that under a given set of ambient conditions all coexisting polymorphs will tend to evolve into the most thermodynamically stable one. Thus, unless this conversion is hindered by a sufficiently high kinetic barrier, changes in the properties and performance of a product may also be observed as time goes by.

The advent of high throughput crystallography allowed the fast buildup of the Cambridge Database (CSD),[12] which emerged as a very powerful tool to analyze how changes in a molecular framework may lead to different types of polymorphism.[5] No equivalent compilation exists, however, for thermodynamic and kinetic data, perhaps because phenomena such as metastability, often make that information comparatively more difficult to acquire experimentally and organize in a database, with appropriate accuracy.[13,14]

Important theoretical advances in areas such as crystal structure prediction[15−20] and molecular dynamics simulations[21] are helping to close this gap and uncover the thermodynamic and kinetic factors that govern polymorph formation and stability. Theoretical predictions still face, however, considerable accuracy limitations,[16−20] given the small energy differences that separate most polymorphs and the difficulty in simulating polymorphic transitions.[21]

Significant steps have also been taken in the experimental front, such as the application of single-particle resolution video microscopy to unveil phase-transition pathways in colloidal crystals,[22,23] or the real-time observation of the heterogeneous nucleation of molecules from solution by atomic-resolution transmission electron microscopy (AR-TEM).[24] Colloidal crystals are, however, still remote from true organic crystals, since they consist of self-assembled structures of colloidal particles (which are already supramolecular aggregates) suspended in liquid media. Also, at present, the use of AR-TEM to study dynamic processes in organic molecular solids is hindered by the rapid decomposition of the samples under electron irradiation.[24] Thus, to the best of our knowledge, the possibility of following solid−solid transitions in organic materials, with enough spatial and temporal resolution to evidence their underlying molecular processes, is still waiting for new technological breakthroughs. It is, therefore, not surprising that many solid−solid transition mechanisms have been proposed (Mnyukh refers to more than 160 in his 2001 book, p 13 and Appendix 1),[10] although, most often, the transformations are considered to follow either a diffusionless (martensitic) pathway,[25,26] involving concerted movements of the molecules, or a diffusive nucleation and growth mechanism,[10] consisting in the formation of one or more stable nuclei of the daughter phase, which feed on the mother phase to propagate the transformation across the crystal. The existence of true concerted diffusionless transitions is, however, still a matter of debate.[10,21,27−29]

In this context, a combined experimental and theoretical approach to polymorphism comprising structural, thermodynamic, and kinetic perspectives, and relying on families of compounds with systematic differences in molecular structure seems particularly interesting for two main reasons: (i) to provide experimental evidence of how specific alterations in a molecular framework impact on packing patterns, stability relationships, and dynamics of transformation between different forms; (ii) to offer a series of sufficiently accurate experimental data that can serve as benchmarks for the validation and refinement of theoretical models used in the investigation of polymorphism. This led us to embark on the study of the $HOC_6H_4C(O)R$ (R = H, *n*-alkyl) family, where the molecular structures differ solely by the length of the R alkyl group chain, and for which, at the outset (around 2007), no prior detection of polymorphism had been reported, albeit individual structures existed for R = H,[30] CH_3,[31] C_3H_7,[32] and C_4H_9.[33]

A crystal engineering rationale suggested that, regardless of the possible existence multiple crystal forms, a common tendency toward a molecular packing based on one-dimensional $C_1^1(8)$ chains sustained by a OH···O═C hydrogen bond motif should be expected for the whole family. This could indeed be confirmed by the available data (R = H,[30] CH_3,[31] C_3H_7,[32] and C_4H_9).[33] However, more subtle aspects such as the impact of differences in molecular conformation (e.g., OH and CO groups in *E* or *Z* conformation) and alkyl chain length, and flexibility, in the conceivable formation of distinct polymorphs were not predictable.

Since then, polymorphs have been isolated in a reproducible way for 4′-hydroxybenzaldehyde (HBA, R = H, forms I[30,34] and II[34,35]) and 4′-hydroxyacetophenone (HAP, R = CH_3, forms I[36,37] and II[31,36−39]). In all cases, the above-mentioned $C_1^1(8)$ chain was found to be present. However, while in HBA, the differences between polymorphs were merely due to adjustments of packing architecture;[34] in HAP changes in molecular conformation (relative orientation of the OH and CO groups) and number of molecules in the asymmetric unit also occurred.[36] Characterization of the two systems in terms of stability domains and dynamics of transformation showed that, despite the distinct structural features behind polymorphism, in both cases:[8,34,36] (i) the two forms were enantiotropically related; (ii) their lattice energy differences were very similar and small (ca. 0.5 kJ·mol^{-1});[34,36] and (iii) in spite of the enantiotropic character, a reversible polymorphic transition in the solid state could not be observed (the transition was only detectable on heating) due to a high activation barrier.[8,34] HAP was also shown to form hydrates[40,41] and to exhibit a unique cooling crystallization behavior in water, where the formation of a hydrate or an anhydrous phase could be mediated by an emulsion.[41,42]

These results suggested that other members of the $HOC_6H_4C(O)R$ family should be prone to polymorphism, and indeed a recent thermal analysis study gave a strong indication that a second crystal form (form II) existed for 4′-hydroxyvalerophenone (HVP, R = C_4H_9, Figure 1), although a structure elucidation was not possible due to the lack of crystals suitable for a single crystal X-ray diffraction (SCXRD)

https://dx.doi.org/10.1021/acs.cgd.9b01481
Cryst. Growth Des. 2020, 20, 2321−2336

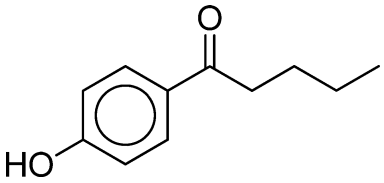

Figure 1. Molecular structure of 4′-hydroxyvalerophenone (HVP), 1-(4-hydroxyphenyl)penta-1-one, CAS number: 2598-71-7.

analysis.[43] This problem was overcome in the present work, which also revealed that a third HVP polymorph (form III) could be obtained through a reversible single crystal to single crystal II ↔ III phase transition. Here we report the structural characterization of the two new HVP polymorphs by single crystal X-ray diffraction and analyze their stability domains, relative stability versus form I, and interconversion dynamics, by using a combination of experimental and molecular dynamics (MD) simulation studies. Finally, on the basis of this approach, it was also possible to suggest a rationalization for why HVP crystallization from melt preferentially leads to form II rather than the more stable form I.

MATERIALS AND METHODS

Materials. The HVP starting material (Tokyo Chemical Industry, mass fraction 0.993) was the same as previously used in a thermochemical study of HOC_6H_4COR (R = H, CH_3, C_2H_5, n-C_3H_7, n-C_4H_9, n-C_5H_{11}, and n-C_6H_{13}) compounds.[44] It had been purified by crystallization from ethanol and characterized in terms of chemical purity and phase purity by elemental analysis, HPLC-ESI/MS, ^{1}H NMR, powder X-ray diffraction (PXRD), and differential scanning calorimetry (DSC). HPLC-ESI/MS assays indicated a mass fraction purity of 0.99999. Comparison of the PXRD pattern recorded at 298 ± 2 K with analogous SCXRD results[12,33,44] showed that the sample corresponded to form I HVP.

Crystals of form I suitable for the SCXRD structural determination carried out in this work at 167 ± 2 K were obtained by crystallization from ethanol (ChemLab, mass fraction 0.998). A saturated solution of HVP in 25 cm^3 of ethanol was prepared at 328 K, filtered while still warm, and the liquid filtrate stored at 255 K. Crystals were formed within 4 days. They were then separated from the mother liquor by vacuum filtration and dried in air at 293 ± 2 K.

Form II was produced by crystallization from the melt. It corresponds to a metastable phase and needs to be handled with care to avoid conversion into form I. A stability test showed that a form II sample obtained by melting form I in an oven and cooling the liquid to ambient temperature could persist without signs of transformation for at least 3 days, if kept untouched under normal laboratory conditions (293 ± 2 K, 1 bar, relative humidity 40% ≤ Φ ≤ 60%). Conversion to form I, was, however, greatly accelerated (the process being completed in one to a few hours) if the sample was subjected to mechanical stress (e.g., grinding with pestle and mortar or scratching with a spatula). To obtain form II crystals suitable for SCXRD, a form I sample was placed in a glass microscopy slide and transferred to a Linkam LTS350 hot stage adapted to an Olympus SZX10 stereo microscope. It was then

Table 1. Crystal Data and Structure Refinement Parameters for the Polymorphs of 4′-Hydroxyvalerophenone at Different Temperatures

polymorph	Form III	Form III	Form II	Form I	Form I[a]
CCDC identifier	1961729	1961731	1961730	1961728	KERPUT
T/K	194 ± 2	222 ± 2	296 ± 2	167 ± 2	298 ± 2
crystal size/mm	0.50 × 0.25 × 0.25	0.60 × 0.44 × 0.39	0.55 × 0.37 × 0.20	0.60 × 0.25 × 0.20	0.30 × 0.20 × 0.20
crystal color	colorless	colorless	colorless	colorless	colorless
crystal system	monoclinic	monoclinic	monoclinic	monoclinic	monoclinic
space group	$C2/c$	$C2/c$	$C2/c$	$P2_1/c$	$P2_1/c$
a/Å	16.828(5)	17.019(7)	19.077(6)	9.9230(11)	9.990(2)
b/Å	8.763(2)	8.745(4)	8.229(2)	10.2539(10)	10.454(2)
c/Å	13.845(4)	13.980(6)	14.227(4)	9.8468(11)	9.882(2)
β/deg	110.629(11)	110.644(12)	111.205(9)	107.183(6)	107.46(3)
V/Å^3	1910.8(10)	1947.0(14)	2082.2(11)	957.19(18)	984.5(4)
Z/Z'	8/1	8/1	8/1	4/1	4/1
ρ_{calc}/g·cm^{-3}	1.239	1.216	1.137	1.237	1.202
μ/mm^{-1}	0.084	0.082	0.077	0.084	
$F(000)$	768	768	768	384	
θ limits/deg	2.660−26.099	2.657−26.089	2.290−26.146	3.241−28.962	
limiting indices	$-17 \le h \le 20$	$-20 \le h \le 20$	$-23 \le h \le 23$	$-13 \le h \le 12$	
	$-10 \le k \le 10$	$-10 \le k \le 10$	$-10 \le k \le 10$	$-13 \le k \le 9$	
	$-17 \le l \le 17$	$-15 \le l \le 12$	$-13 \le l \le 17$	$-13 \le l \le 13$	
no. of refns collected/ unique	3012/1741 [R(int) = 0.0197]	5683/1666 [R(int) = 0.0411]	6718/1987 [R(int) = 0.0582]	8640/2535 [R(int) = 0.0505]	
completeness to θ (%)	91.5	86.1	96.4	99.8	
data/restraints/parameters	1741/0/174	1666/0/174	1987/0/174	2535/0/174	
GOF on F^2	1.023	1.013	0.960	0.985	
final R indices [$I > 2\sigma(I)$]	R_1 = 0.0570	R_1 = 0.0450	R_1 = 0.0639	R_1 = 0.0484	
	R_2 = 0.1363	R_2 = 0.1070	R_2 = 0.1726	R_2 = 0.1153	
R indices (all data)	R_1 = 0.1062	R_1 = 0.0817	R_1 = 0.1447	R_1 = 0.0827	
	R_2 = 0.1517	R_2 = 0.1264	R_2 = 0.2020	R_2 = 0.1283	
largest diff peak and hole/ e·Å^{-3}	0.247 and −0.201	0.191 and −0.181	0.170 and −0.166	0.247 and −0.235	
packing index	70.8	69.3	64.7	71.0	69.0

[a]Data from ref 33, except for the packing index which was calculated in this work.

https://dx.doi.org/10.1021/acs.cgd.9b01481
Cryst. Growth Des. 2020, 20, 2321−2336

thermally treated according to the following program: (i) heating to 358 at 5 K·min^{-1}; (ii) 10 min isothermal step; (iii) cooling to 296 at 5 K·min^{-1}. The crystals were gently cropped with a blade, coated with Paratone-N oil, mounted on a Kapton loop, and transferred to the diffractometer.

The finding that the III ↔ II transition can readily occur in both directions under single crystal to single crystal conditions allowed the determination of the form III structure by SCXRD. For this purpose, form III was prepared *in situ*, by cooling a form II crystal mounted in the diffractometer below ∼248 K.

Single Crystal X-ray Diffraction (SCXRD). Single crystal X-ray diffraction studies were performed in a Bruker AXS-KAPPA APEX II or a D8 Quest area detector diffractometer. Graphite-monochromated Mo Kα (λ = 0.71073 Å) radiation sources running at 50 kV and 30 mA were used in both instruments. The crystals were coated with Paratone-N oil and mounted on a Kapton loop. An empirical absorption correction was enforced using Bruker SADABS,[45] and data reduction was done with Bruker SAINT.[46] The structures were solved by direct methods with Bruker SHELXS[47] and refined by full-matrix-least-squares on F^2 using SHELXL,[47] both programs included in WINGX-Version 2014.1.[48] Non-hydrogen atoms were refined with anisotropic thermal parameters. Hydrogen atoms were located on the density map and isotropic displacement parameters, U_{iso}(H), refined freely. Structural representations were made with Mercury 3.8,[49] and PLATON was used for the hydrogen bond (H-bond) interactions and packing index.[50] A summary of the crystal data, structure solution, and refinement parameters is given in Table 1. It should be noted that only weakly diffracting form II and form III crystals could be produced. This justifies the low quality of the SCXRD data obtained for these two forms compared to form I.

Differential Scanning Calorimetry (DSC). DSC scans in the range 193−353 K were carried out with a TA Instruments 2920 MTDSC apparatus equipped with a refrigerated cooling accessory (LNCA) that provided automatic and continuous programmed sample cooling down to 123 K. The samples with ∼5.0 mg mass were contained in aluminum pans, sealed in air. All the measurements were done under helium (Air Liquide N55), at a flow rate of 30 cm^3·min^{-1}, using a heating rate of 5 K·min^{-1}. Calibration of the temperature scale of the instrument was based on the fusion temperatures, T_{fus}, of *n*-decane (T_{fus} = 243.75 K), *n*-octadecane (T_{fus} = 301.77 K), hexatriacontane (T_{fus} = 347.30 K), indium (T_{fus} = 430.61 K), and tin (T_{fus} = 506.03 K). The heat flow scale was calibrated by using indium ($\Delta_{fus}h$ = 28.71 J·g^{-1}). All weightings were performed with a precision of ±0.1 μg in a Mettler UMT2 ultramicro balance.

Heat capacity determinations on HVP form II were made on a 204 F1-Phoenix DSC from Netzsch, using a previously described procedure.[51,52] Details are given as Supporting Information.

Microscopy. Hot stage polarized optical microscopy (HSM) studies of the III → II phase transition were performed with an Olympus BX51 microscope equipped with a Linkam LTS360 liquid nitrogen-cooled cryostage and a Linkam TMS94 programmable temperature controller. The microstructure of the sample was monitored with an Olympus C5060 wide zoom camera. Images were recorded with 250× magnification. The HVP sample was placed between two microscope slides and inserted into the hot stage. It was then subjected to the following temperature program at a heating/cooling rate of 10 K·min^{-1}: (i) heating from 298 to 343 K (∼10 K above fusion); (ii) cooling to 193 K; (iii) heating to 273 K. The occurrence of the II → I phase transition induced by mechanical stress was investigated at 293 ± 2 K, with a BIJIA Electronic U600X monocular USB microscope controlled by the in-house developed CB-MScope 01 software.[53]

Molecular Dynamic (MD) Simulations. MD simulations on the HVP solid phases were carried out with LAMMPS (18 Sep. 2018).[54] GROMACS 2016.4[55] was used for the liquid phase. A cutoff distance of 15 Å was selected for all calculations. Interactions beyond this limit were computed by the particle-Mesh Ewald electrostatics method. The simulations of the solid state were performed under an anisotropic isothermal−isobaric ensemble ($N-\sigma-T$), using a Nose-Hoover thermostat and barostat (relaxation time constants of 0.2 and 2 ps, respectively) to control temperature and pressure. For the liquid phase, an isotropic isothermal−isobaric ensemble ($N-P-T$) was selected. In this case, temperature and pressure control were ensured by a V-rescale thermostat (1 ps time constant) and a Parrinello−Rahman barostat (10 ps time constant; compressibility components set to 1 × 10^{-5} bar^{-1}), respectively. The temperature of each simulation was set as indicated below and, unless otherwise stated, the pressure was 1 bar.

The simulation boxes for the crystal phases were built by stacking several unit cells along the three cell axes: form I, 4 × 4 × 4, 256 molecules, 6912 atoms; forms II and III, 2 × 5 × 3, 240 molecules, 6480 atoms. In the case of forms I and II, the MD runs involved two steps: (i) first the initial configuration was heated from 10 to 298 K in 2 ns; (ii) this was followed by a 4 ns production stage at 298 K, where the configuration of the simulation box was recorded every 2 ps. In the case of form III: (i) the starting configuration was initially heated from 10 to 150 K during 2 ns, followed by a 4 ns production stage at the final temperature; (ii) the crystal was then heated at 10 K·ns^{-1} up to 210 K. Between 170 and 180 K, the configuration of the simulation box was recorded every 0.01 ps. Below and above this range, data were collected in 2 ps intervals. A time step of 1 fs was used for all three HVP solid forms.

The simulation of liquid HVP was initiated by placing 500 molecules (13 500 atoms) in a cubic box with 500 Å side. A 20 ns MD run was subsequently performed at 500 K and 100 bar. Then several 10 ns simulations were carried out at 1 bar and 350 K (∼15 K above the fusion temperature of form I, T_{fus} = 335.2 ± 0.2 K, experimentally determined by DSC, see below) until a constant density of the liquid (1009.2 ± 4.1 kg·m^{-3}) was achieved. Finally, a production stage of 40 ns at 1 bar and 350 K was made, where the configuration of the simulation box was recorded every 2 ps. In this case a 2 fs time step was selected. To ensure that the final structure of liquid HVP corresponded to a properly equilibrated phase, the previous procedure was repeated twice, starting the simulation with the molecules in different positions and orientations inside the box.

The force field used for the MD simulations was built by taking the van der Waals parameters and the potential functions for bonds, angles, and dihedrals, from the OPLS-AA model.[56,57] Atomic point charges (APCs) were first computed by the ChelpG methodology[58] at the MP2/aug-cc-pVDZ level of theory,[59−63] using the following procedure: (i) optimization of a single HVP molecule in the gaseous phase, with the OH and CO groups in both *E* and *Z* conformations; (ii) computation of APCs for the two configurations; (iii) evaluation of an average APC for atoms in equivalent positions. This approach was attempted since recent work had suggested that a significant improvement in the accuracy of crystal structure simulations could be achieved by using the OPLS-AA parametrization coupled with atomic point charges (APC) obtained from quantum chemistry methods.[64,65] The above procedure led, however, to unreasonable APC values for the hydrogen and carbon atoms in the alkyl chain (e.g., hydrogen atoms with negative charges). As such, the APCs for CH_2 and CH_3 groups in the alkyl chain were also taken from the OPLS-AA database, and the ChelpG charges of the remaining atoms were adjusted by evenly distributing the overcharge, so that the electroneutrality of the molecule could be ensured. This led to a significant improvement in the accuracy of the predicted structural data, when compared with computations relying on charges obtained from step (iii). A ∼12% improvement was, for example, observed in the case of the *b* unit cell dimension of form I. The final parametrization used in the simulations is given as Supporting Information (Table S8).

The input files necessary to run GROMACS and LAMMPS simulations were prepared with DLPGEN 3.0.[64] The molecular arrangements in the solid and liquid phases were investigated through First Shell Analysis (FSA) and Combined Distribution Functions (CDF) computed using the program AGGREGATES.[66] Illustrations and videos of the simulation boxes were made with VMD.[67] All ab initio calculations were performed using the Gaussian 09 D.01 package.[68]

RESULTS AND DISCUSSION

Differential Scanning Calorimetry. Typical differential scanning calorimetry profiles obtained by subjecting an HVP sample to a series of cooling−heating runs in the range 193−353

https://dx.doi.org/10.1021/acs.cgd.9b01481
Cryst. Growth Des. 2020, 20, 2321−2336

K are shown in Figure 2 (detailed results are given as Supporting Information). When form I was cooled to 210 K and

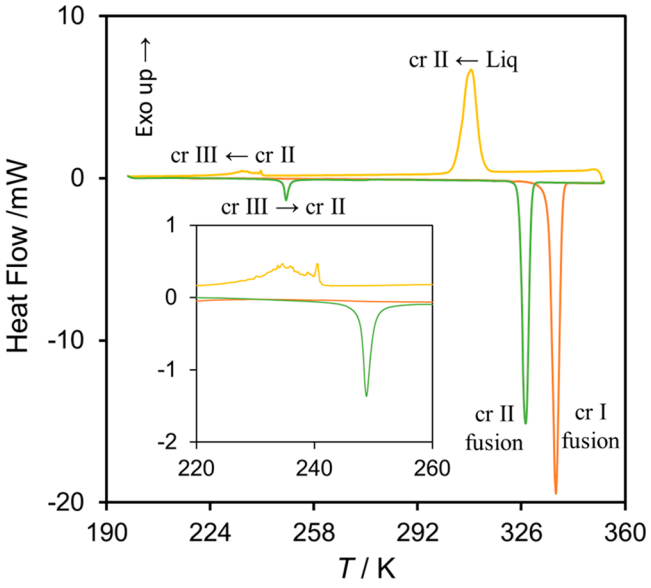

Figure 2. DSC profile obtained by subjecting HVP to a three-step program at a heating/cooling rate of 5 K·min^{-1}: Step 1 (orange), heating of form I from 210 to 353 K; Step 2 (yellow), cooling the melted sample from 353 to 193 K; Step 3 (green), heating the cooled sample from 193 to 353 K. The inset shows a detailed view of the III ↔ II reversible phase transition.

subsequently heated to 353 K (Figure 2, orange line), no thermal event other than fusion was detected. The corresponding onset temperature, T_{on}, standard molar enthalpy, $\Delta_{fus}H^{o}_{m}$(cr I), and standard molar entropy, $\Delta_{fus}S^{o}_{m}$(cr I), of fusion were T_{on} = 335.2 ± 0.2 K, $\Delta_{fus}H^{o}_{m}$(cr I) = 26.7 ± 0.8 kJ·mol^{-1}, and $\Delta_{fus}S^{o}_{m}$(cr I) = 79.7 ± 2.4 J·K^{-1}·mol^{-1} (cr denotes a crystal form). This behavior had been previously observed for form I and the presently obtained temperature, enthalpy, and entropy data are in excellent agreement with the reported T_{on}= 335.6 ± 0.7 K, $\Delta_{fus}H^{o}_{m}$(cr I) = 26.67 ± 0.04 kJ·mol^{-1}, and $\Delta_{fus}S^{o}_{m}$(cr I) = 79.5 ± 0.2 J·K^{-1}·mol^{-1}.[43]

On cooling the liquid to 193 K (Figure 2, yellow line), two exothermic events were noted. Their nature could subsequently be assigned based on single crystal X-ray diffraction analysis (see below). First, a sharp peak corresponding to the crystallization of form II was detected (T_{on} = 313.2 ± 0.2 K, $\Delta_{cryst}H^{o}_{m}$ = −18.0 ± 0.4 kJ·mol^{-1} and $\Delta_{cryst}S^{o}_{m}$ = −57.5 ± 1.3 J·K^{-1}·mol^{-1}). This was followed by a second wide peak, covering a ∼30 K range, due to the conversion of form II to a previously unknown HVP polymorph, here dubbed form III (T_{on} = 239.1 ± 2.6 K, $\Delta_{trs}H^{o}_{m}$ = −1.5 ± 0.1 kJ·mol^{-1}, and $\Delta_{trs}S^{o}_{m}$ = −6.3 ± 0.3 J·K^{-1}·mol^{-1}). The crystallization of form II from the melt had been previously observed by DSC, although crystals suitable for a structural determination by SCXRD could not be produced at that time.[43] These experiments also failed to show the formation of form III. The III ↔ II transition was found to be reversible, as form III converted to form II on heating (Figure 2, green line), with T_{on} = 247.5 ± 0.4 K, $\Delta_{trs}H^{o}_{m}$ = 1.5 ± 0.2 kJ·mol^{-1}, and $\Delta_{trs}S^{o}_{m}$ = 6.0 ± 0.8 J·K^{-1}·mol^{-1}. It is interesting to note that despite the 8.4 K difference in onset temperatures (metastable zone width), the absolute values of $\Delta_{trs}H^{o}_{m}$ and $\Delta_{trs}S^{o}_{m}$ obtained on cooling and on heating modes are remarkably similar. This gives a good indication that the phase transition is fully completed on descending or ascending the temperature.

Further heating of form II led to fusion with T_{on} = 325.6 ± 0.3 K, $\Delta_{fus}H^{o}_{m}$(cr II) = 18.9 ± 0.3 kJ·mol^{-1}, and $\Delta_{fus}S^{o}_{m}$(cr II) = 58.1 ± 1.0 J·K^{-1}·mol^{-1}. These values are very close to the previously reported T_{on} = 324.3 ± 0.2 K, $\Delta_{fus}H^{o}_{m}$(cr II) = 18.14 ± 0.18 kJ·mol^{-1}, and $\Delta_{fus}S^{o}_{m}$(cr II) = 55.9 ± 0.5 J·K^{-1}·mol^{-1}.[43] The fact that, in absolute terms, they are in agreement with the above-mentioned $\Delta_{cryst}H^{o}_{m}$ = −18.0 ± 0.4 kJ·mol^{-1} and $\Delta_{cryst}S^{o}_{m}$ = −57.5 ± 1.3 J·K^{-1}·mol^{-1}, also suggests that crystallization of form II from the melt is a complete process.

The DSC results suggest that forms II and III are enantiotropically related and that form II is monotropic relative to form I. The monotropic relationship between forms II and I had been previously advanced based on Burger and Ramberger's heat of fusion rule,[69] given that form I has both a higher temperature of fusion and a higher enthalpy of fusion than form II.[43] The conclusion that form I is more stable than form II in the temperature range covered by the DSC experiments (193−353 K) is also supported by the following observations: (i) form I showed no evidence of conversion into form II in slurry tests carried out in the range 283−312 K using ethyl acetate as solvent; (ii) spontaneous conversion of form II to form I at 296 K could be induced by gentle grinding with a pestle and mortar or scratching a sample with a spatula; (iii) when form II contained in a DSC crucible was gently crushed with a spatula before the run, the pattern corresponding to the red line in Figure 3 was obtained, where form II melting is followed by recrystallization into form I that subsequently undergoes fusion.

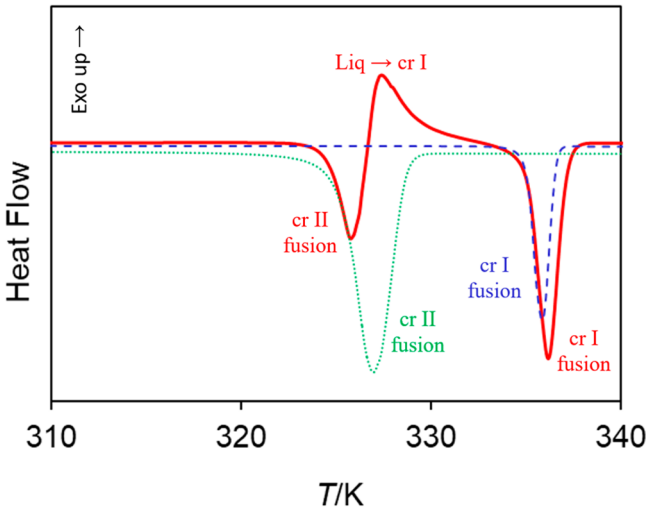

Figure 3. Overlay of the DSC fusion profiles of pure forms I (blue dashed line) and II (green dotted line) with that of a form II sample gently crushed with a spatula inside the crucible (red solid line).

Relative Stability of HVP Polymorphs. The enthalpy and entropy results mentioned above, together with heat capacity data for form I and liquid HVP retrieved from the literature[44] and measured in this work for form II by DSC (see Supporting Information), allowed an evaluation of the relative stabilities of the three HVP polymorphs at 298 K, based on the entropies, enthalpies, and Gibbs energies of conversion of forms II and III into form I, estimated as described in the Supporting Information. The obtained $\Delta_{trs}H^{o}_{m}$, $\Delta_{trs}S^{o}_{m}$, and $\Delta_{trs}G^{o}_{m}$ values are summarized in Table 2.

https://dx.doi.org/10.1021/acs.cgd.9b01481
Cryst. Growth Des. 2020, 20, 2321−2336

Table 2. Enthalpies, Entropies, and Gibbs Energies for the Conversion of HVP Forms III and II into Form I, at 298 K

transition	$\Delta_{trs}H^{o}_{m}$/ kJ·mol^{-1}	$\Delta_{trs}S^{o}_{m}$/J·K^{-1}· mol^{-1}	$\Delta_{trs}G^{o}_{m}$/ kJ·mol^{-1}
Form II → Form I	−6.5 ± 0.9	−19.0 ± 2.6	−0.8 ± 1.2
Form III → Form I	−5.0 ± 0.9	−13.0 ± 2.7	−1.1 ± 1.2

The contribution of the lattice enthalpy, $\Delta_{lat}H^{o}_{m}$, for the relative stabilities of the three HVP forms at 298 K was also evaluated, based on $\Delta_{lat}H^{o}_{m}$(cr I) = 125.9 ± 0.6 kJ·mol−[1],[44] $\Delta_{lat}H^{o}_{m}$(cr II) = 119.4 ± 1.1 kJ·mol^{-1}, and $\Delta_{lat}H^{o}_{m}$(cr III) = 120.9 ± 1.1 kJ·mol^{-1}. For all HVP polymorphs, $\Delta_{lat}H^{o}_{m}$ at 298 K was taken as the enthalpy change associated with the process:

$$\text{HVP(cr)} \rightarrow \text{HVP(g)} \quad (1)$$

where the crystal lattice is destroyed to yield HVP in the ideal gas state.[8,51] It can, therefore, be identified with the enthalpy of sublimation at 298 K, namely, $\Delta_{lat}H^{o}_{m} = \Delta_{sub}H^{o}_{m}$. In the case of form I, $\Delta_{sub}H^{o}_{m}$(cr I) = 125.9 ± 0.6 kJ·mol^{-1} at 298 K had been previously reported.[44] The enthalpies of sublimation of forms II and III (hence their lattice enthalpies) were obtained from

$$\Delta_{sub}H^{o}_{m} = \Delta_{sub}H^{o}_{m}(\text{cr I}) + \Delta_{trs}H^{o}_{m} \quad (2)$$

where $\Delta_{trs}H^{o}_{m}$ refers to either the $\Delta_{trs}H^{o}_{m}$(II → I) or $\Delta_{trs}H^{o}_{m}$(III → I) = $\Delta_{trs}H^{o}_{m}$(III → II) − $\Delta_{trs}H^{o}_{m}$(II → I) values in Table 2.

The comparison of the $\Delta_{trs}G^{o}_{m}$ and $\Delta_{trs}H^{o}_{m}$ trends in Table 2 suggests that a larger lattice enthalpy does not necessarily translate into a higher thermodynamic stability. Indeed, while the lattice enthalpies of the HVP polymorphs, at 298 K, decrease according to form I > form III > form II the stability order at the same temperature deduced from the $\Delta_{trs}G^{o}_{m}$ values in Table 2 is form I > form II > form III. This stresses two important points: (i) the lattice enthalpy may not be a reliable indicator of the relative stability of polymorphs when (as often happens) the forms under consideration are separated by small enthalpy differences; (ii) entropic factors can play a determinant role in the stabilization of polymorphs and should ideally be accounted for in computational analysis of polymorphic landscapes and polymorphic phase transitions. This is, however, still a challenge.[70−72] It may finally be pointed out that the above conclusions regarding the relative stabilities of HVP forms I to III are expected to hold, in spite of the approximations involved in the calculations of $\Delta_{trs}H^{o}_{m}$, $\Delta_{trs}S^{o}_{m}$, and $\Delta_{trs}G^{o}_{m}$ in Table 2 (see Supporting Information). First, the observation of a spontaneous III → II enantitropic transformation quite below 298 K (247.5 K) and of the monotropic II → I conversion at ambient temperature upon gentle grinding gives a clear indication that G^{o}_{m}(cr III) > G^{o}_{m}(cr II) > G^{o}_{m}(cr I) at 298 K. Second, the lattice enthalpy order form I > form III > form II was still maintained when: (i) ± 10% variations in the standard molar heat capacities ($C^{o}_{p,m}$) of form I, form II, and liquid HVP implicated in the calculation of $\Delta_{trs}H^{o}_{m}$(II → I) at 298 K were considered; and (ii)

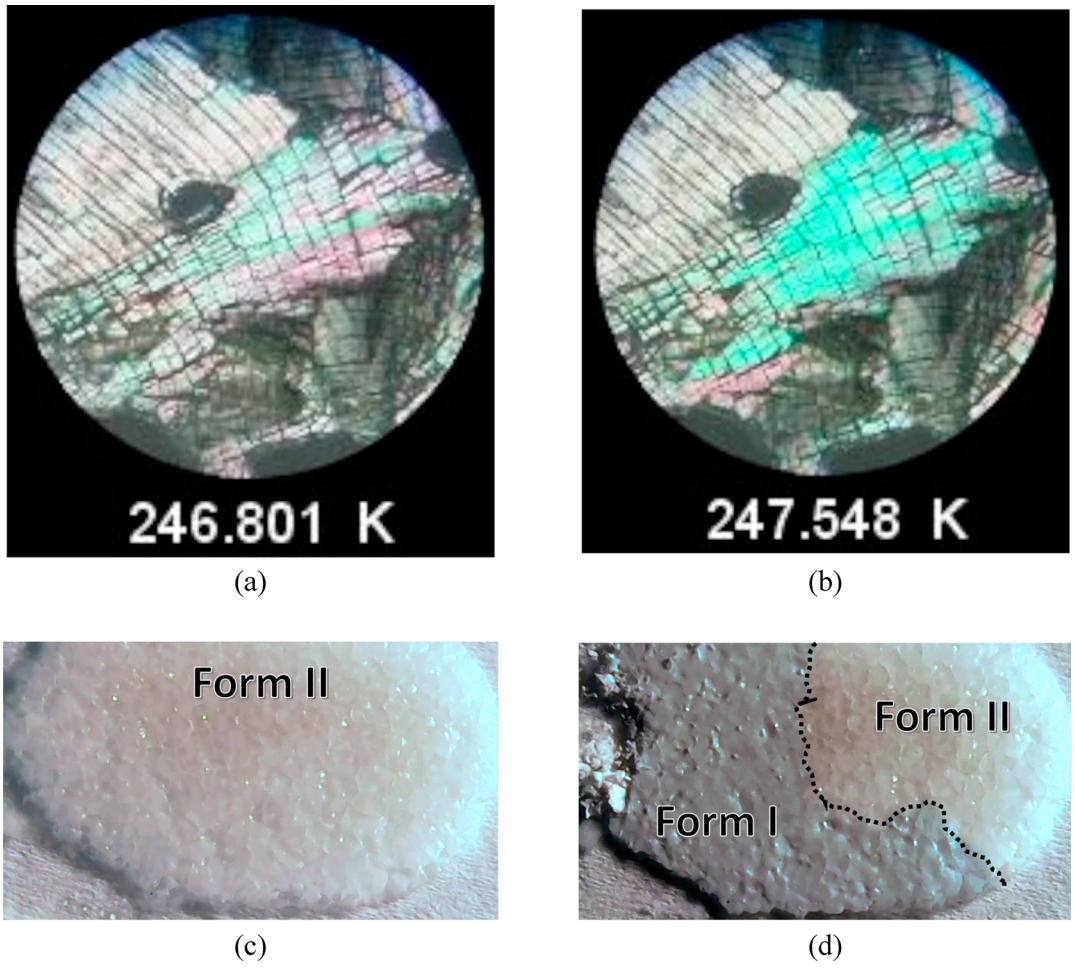

Figure 4. Microscopy images of HVP: (a) before and (b) after the III → II phase transition; (c) before and (d) during the II → I transformation.

https://dx.doi.org/10.1021/acs.cgd.9b01481
Cryst. Growth Des. 2020, 20, 2321−2336

$\Delta_{trs}C^{o}_{p,m}$(III → II) used in the estimation of $\Delta_{trs}H^{o}_{m}$(III → II) at 298 K, that precedes the calculation of $\Delta_{trs}H^{o}_{m}$(III → I) at this same temperature as $\Delta_{trs}H^{o}_{m}$(III → I) = $\Delta_{trs}H^{o}_{m}$(III → II) − $\Delta_{trs}H^{o}_{m}$(II → I), was increased from 0 $J{\cdot}K^{-1}{\cdot}mol^{-1}$ (as assumed here, given the structural similarity between both phases) to 20 $J{\cdot}K^{-1}{\cdot}mol^{-1}$.

Microscopy. The occurrence of the III → II transition and its reversible character were further evidenced by hot-stage microscopy. On heating form III from 193 to 273 K, changes in the interference colors transmitted by the sample were clearly noted at ∼247 K (Figure 4a,b and video 1 given as Supporting Information). This value closely matches the temperature of the III → II phase transition given by the DSC experiments (T_{on} = 247.5 ± 0.4 K). The interference color changes are accompanied by modifications in the shape/size of the microcrystallites, which are likely to reflect the differences in the unit cell dimensions of forms III and II shown in Table 1. A reverse behavior is observed on cooling, with the transition noted at ∼244 K, which compares well with 239 K observed in the DSC experiments. The HSM study also indicated that the transition is fast in both directions and seems to proceed by a sudden lattice contraction/expansion, without any apparent development of an interface propagating throughout the sample. This suggests that the transformation occurs by an overall cooperative molecular movement, rather than by diffusive nucleation and growth, a conclusion that was further supported by the MD simulation results discussed below.

Microscopy imaging using the BIJIA USB apparatus corroborated the above-mentioned spontaneous conversion of form II to form I induced by a mechanical stimulus. As shown in Figure 4c,d (see also video 2 given as Supporting Information), grinding a peripheric zone of a polycrystalline form II sample (obtained by crystallization from the melt) led to the development of a transition front that quickly extended to the whole material. A diffusive nucleation and growth mechanism is, therefore, likely to be operative in this case.

The different behaviors observed for the III → II and II → I transformations are consistent with the single crystal X-ray diffraction results discussed in the next section, showing that the former requires only a small rearrangement of the molecules in the crystal lattice, without any change in the crystal system (monoclinic) or space group ($C2/c$), while the latter implies modifications in space group ($C2/c$ to $P2_1/c$), molecular conformation (the relative orientations of the CO and OH groups change from and Z in form II to E in form I), and morphology of the $C_1^1(8)$ chain that constitutes the main 1D packing motif (planar to "herringbone").

Single Crystal X-ray Diffraction. As mentioned in the Introduction, prior to this work only the structure of form I at 298 ± 2 K (CSD ref code: KERPUT)[12] was known.[33] Evidence for the likely existence of form II was available from thermal analysis results, but the corresponding crystal structure had not been determined, and form III had not been identified.[43] The structural characterization of these two new HVP polymorphs became possible when, in the course of this work, it was found that (i) crystals of form II suitable for SCXRD analysis could be produced by crystallization from the melt and that (ii) it was possible to generate form III by cooling a form II crystal below 247 K (i.e., the II → III phase transition occurs under single crystal to single crystal conditions). Single crystal X-ray diffraction studies were then carried out for form I at 167 ± 2 K, form II at 296 ± 2 K, and form III at 194 ± 2 K and 222 ± 2 K.

As shown in Table 1, all HVP polymorphs are monoclinic, but while forms III and II belong to the $C2/c$ space group, form I is $P2_1/c$. The molecular framework is very similar in all of them, except for the relative orientation of the OH and C═O groups which is Z in form I and E in forms II and III (Figure 5). This

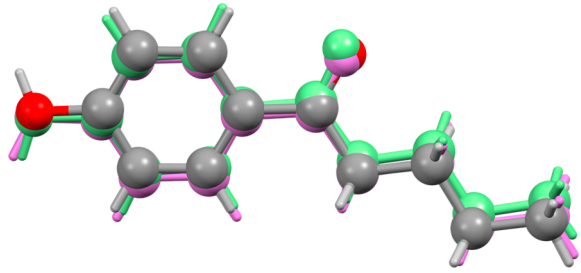

Figure 5. Overlay of the molecular structures of the three 4′-hydroxyvalerophenone polymorphs highlighting the differences in Z (form I) and E (forms II and III) conformations: form I (colored by atom type, 298 K); form II (light green, 296 K); form III (pink, 222 K).

type of conformational polymorphism had been previously found in 4′-hydroxyacetophenone (HAP), where E and Z molecular conformations are present in the high (form I) and low (form II) temperature forms, respectively.[36] In HAP, however, a change in the number of molecules in the asymmetric unit (Z' = 1 in form I and Z' = 2 in form II) also occurs, a feature that is not observed in HVP.

No significant differences were noted when the molecular structure of HVP form I obtained at 167 K was compared with that published[33] at 298 K (see Supporting Information). An overlay of the molecular structures of form III at 194 and 222 K led to an analogous conclusion (see Supporting Information).

The molecular packing of form I at 298 K (Figure 6) displays a "herringbone" type structure formed by $C_1^1(8)$ chains propagating along the b axis, where adjacent molecules are positioned at ∼90°. This motif is sustained by "head-to-tail" OH···O ($d_{OH\cdots O}$= 1.898 Å) hydrogen bonds involving the hydroxyl group of a given molecule and the carbonyl group of the next one. The 3D packing is held by $CH_{ring}\cdots O_{hydroxyl}$ ($d_{CH\cdots O}$ = 2.597 Å), $CH_{alkyl}\cdots O_{carbonyl}$ ($d_{CH\cdots O}$ = 2.706 Å), and $\pi-\pi$ stacking ($d_{\pi-\pi}$ = 3.640 Å) interactions between the $C_1^1(8)$ chains (Figure 6). Decreasing the temperature to 167 K does not lead to significant changes in crystal packing. The unit cell contraction results in shorter OH···O ($d_{OH\cdots O}$ = 1.786 Å), $CH_{ring}\cdots O_{hydroxyl}$ ($d_{CH\cdots O}$ = 2.526 Å), $CH_{alkyl}\cdots O_{carbonyl}$ ($d_{CH\cdots O}$ = 2.615 Å), and $\pi-\pi$ stacking interaction distances ($d_{\pi-\pi}$= 3.596 Å).

The structure of form II (Figure 7a) is also composed of $C_1^1(8)$ infinite chains that propagate along the b axis, supported by "head-to-tail" OH···O ($d_{OH\cdots O}$ = 1.945 Å) hydrogen bonds. In this case, however, the chains are planar, formed by molecules that are parallel to each other. Coplanar $C_1^1(8)$ chains interact along the a axis through $CH_{ring}\cdots O_{hydroxyl}$ ($d_{CH\cdots O}$ = 2.736 Å) nonclassical H-bonds. As shown in Figure 7b, the orientation of the chains in adjacent planes follows an AA′BB′ sequence. The chains in AA′ pairs are rotated by ∼180° relative to each other, and the same is true for BB′. In addition, each AA′ pair makes a ∼90° angle with the corresponding BB′ pair. The 3D framework is ensured by $\pi-\pi$ stacking interactions set at 3.548 Å within AA′ and BB′ pairs and 3.578 Å in the case of A′B and B′A pairs.

Much of the structural features discussed for form II also hold for form III, which displays a packing architecture very similar to that in Figure 7. Some variations in interaction distances can,

https://dx.doi.org/10.1021/acs.cgd.9b01481
Cryst. Growth Des. 2020, 20, 2321−2336

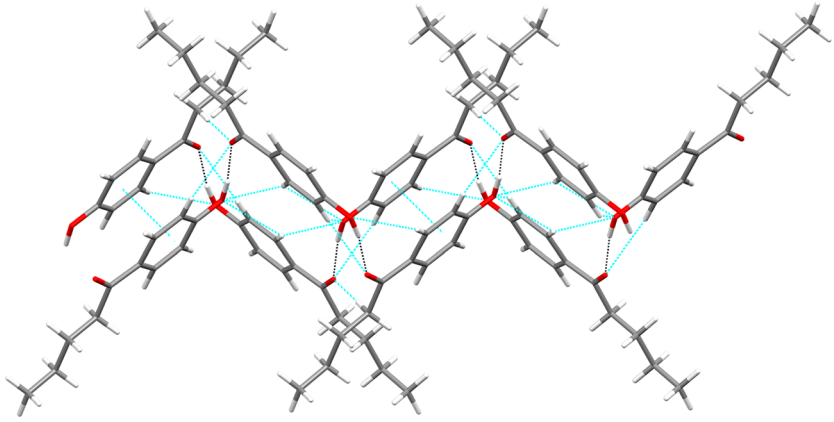

Figure 6. Crystal packing of HVP form I at 298 K[33] showing the "herringbone" type $C_1^1(8)$ chains that propagate along the *b* axis and are sustained by "head-to-tail" OH···O═C hydrogen bonds (black). Also displayed (cian) are the $CH_{ring}\cdots O_{hydroxyl}$, $CH_{alkyl}\cdots O_{carbonyl}$, and $\pi-\pi$ stacking interactions between the chains that hold the 3D packing.

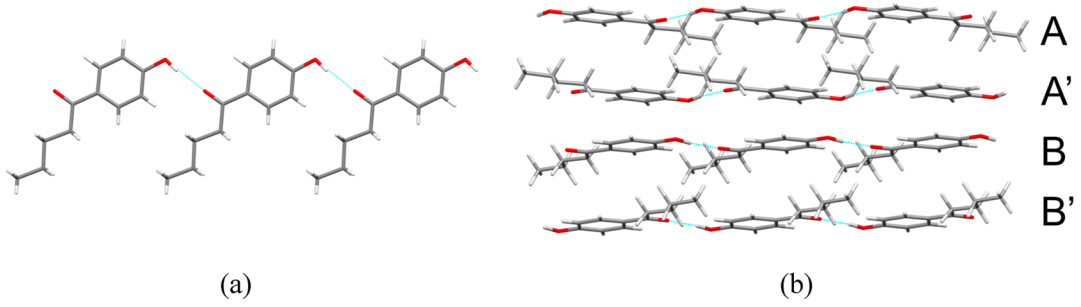

Figure 7. Crystal packing of 4′-hydroxyvalerophenone form II: (a) $C_1^1(8)$ chains showing the molecules parallel to each other; (b) 3D stacking of the $C_1^1(8)$ chains according to a AA′BB′ type sequence. Form III displays very similar packing features.

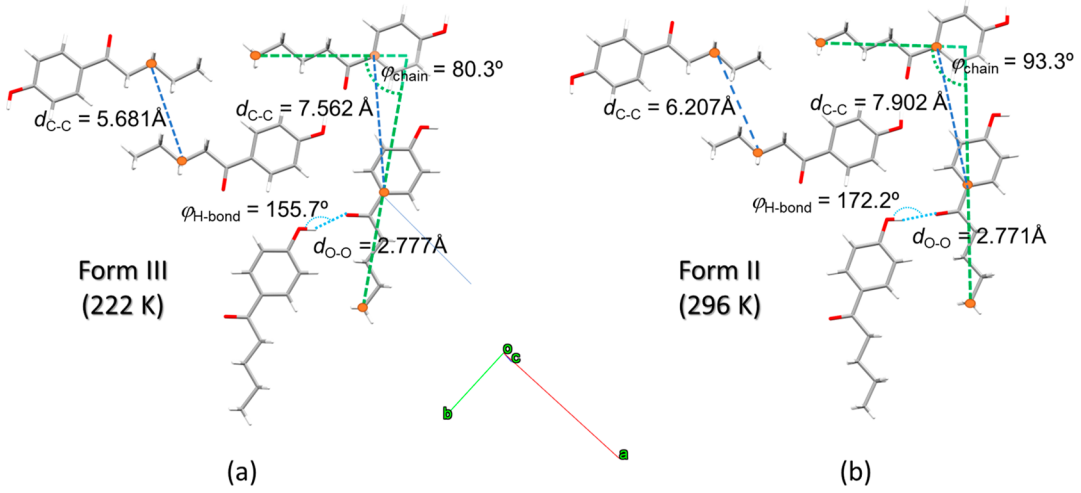

Figure 8. Some significant differences in molecular organization between HVP forms II and III: (a) form III at 222 K and (b) form II at 296 K, viewed perpendicularly to the (−1 0 2) plane.

however, be noted when the structures of forms III (222 K) and II (296 K) are compared: in form III, the OH···O ($d_{OH\cdots O}$ = 1.951 Å) and $\pi-\pi$ stacking ($d_{\pi-\pi}$ = 3.622 Å for the AA′ and BB′ pairs; $d_{\pi-\pi}$= 3.5621 Å for A′B or B′A pairs) contacts become longer and the $CH_{ring}\cdots O_{hydroxyl}$ distances ($d_{CH\cdots O}$ = 2.726 Å) become shorter. The comparison also shows that (Figure 8): (i) the angle between alkyl chains of molecules in adjacent and coplanar $C_1^1(8)$ chains varies from ∼80° (form III) to ∼93° (form II); (ii) the O−H···O hydrogen bond angle increases from 156° in form III to a more favorable 172° value in form II; (iii) the separation of the alkyl chains increases, as can be deduced from the significant elongation (∼0.5 Å) of the distance between the central atoms of adjacent R groups (5.7 Å to 6.2 Å); and (iv) the distance between aromatic carbons linked to −C(O)R groups also increases by ∼0.3 Å (7.6−7.9 Å) when adjacent molecules are considered. These differences are likely to reflect an enhanced conformational and positional freedom of the HVP molecules in the less dense/lower packing index form II. Indeed, as shown in Table 1, the III → II process is accompanied by a ∼6% decrease in both density (1.216 g·cm^{-3}

https://dx.doi.org/10.1021/acs.cgd.9b01481
Cryst. Growth Des. 2020, 20, 2321−2336

in form III at 222 K and 1.145 g·cm^{-3} in form II at 296 K) and packing index (69.3% in form III to 64.7% in form II). Further support for this possible increase in molecular mobility was provided by the MD simulations discussed below.

Table 1 also shows that the interconversion of forms II and III is accompanied by non-negligible changes in unit cell parameters. When the structure of form III at 222 K is compared with that of form II at 296 K, the following modifications are noted: *a* expands by ∼12%, *b* contracts by ∼6%, *c* contracts by ∼1%, and the angle *β* increases by 0.4%. It may be mentioned that these deviations are essentially maintained if the unit cell dimensions of form III are linearly extrapolated to 296 K by using the data at 194 K and 222 K in Table 1: *a* = 17.519 Å (9%), *b* = 8.700 Å (6%), *c* = 14.337 Å (1%), *β* = 110.689° (0.3%).

Despite all the differences noted above, the overlay in Figure 9a clearly shows that there is a considerable packing similarity between forms II and III, thus suggesting that their interconversion can be achieved without a significant rearrangement of the crystal lattice. This is compatible with the observation in the SCXRD experiments that the III ↔ II transition can occur under single crystal to single crystal conditions. It is also in line with the combined DSC and hot stage microscopy evidence, showing that the process is fast and reversible and seems to proceed by a sudden lattice contraction/expansion, without any apparent development of a transition front propagating throughout the sample. The overall SCXRD, DSC, and HSM results, therefore, suggest that the III → II transition probably occurs by a mechanism involving a concerted movement of the molecules that does not require the destruction and reconstruction of the crystal lattice.

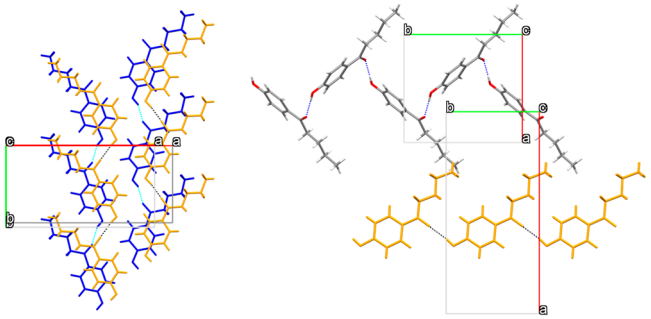

(a) (b)

Figure 9. (a) Overlay of the unit cells of 4′-hydroxyvalerophenone forms III (blue, 222 K) and II (orange, 296 K), showing the changes associated with the enantiotropic III → II phase transition. (b) Analogous overlay for the monotropic II → I phase transition (form II, orange, 296 K; form I, colored by atom, 298 K).

In contrast, as illustrated in Figure 9b, the II → I transformation involves a considerable change in molecular packing, that is likely to be hindered by a significant activation barrier. The observed resilience of the metastable form II in converting to the stable form I at 298 K should, therefore, be related to the difficulty in overcoming this barrier. It may also be pointed out that the larger stability of form I relative to form II, deduced from the DSC measurements, is compatible with the following indications from SCXRD: (i) stronger H-bonds are present in form I ($d_{OH\cdots O}$ are shorter in form I than in form II); (ii) $CH_{ring}\cdots O_{hydroxyl}$ contacts in form II ($d_{CH\cdots O}$ = 2.736 Å) are much longer than in form I ($d_{CH\cdots O}$ = 2.526 Å) and exceed the sum of the O and H van der Waals radii (2.720 Å) given by Mercury 3.8;[49] (iii) the density and packing index are both larger for form I than for form II (Table 1), suggesting a more efficient and effective packing of the HVP molecules in the former than in the latter polymorph.

Polymorphism Across the $HOC_6H_4C(O)R$ (R = H, alkyl) Family. Representative structural and energetic results for HVP, obtained in this work, are compared in Table 3 with the analogous data reported for other members of the $HOC_6H_4C(O)R$ (R = H, *n*-alkyl) family.[30,32,33,35−37,39,44] For the sake of consistency, whenever possible, structural information at ∼298 K was selected. All lattice enthalpies in Table 3 also refer to 298 K.

As already mentioned, the most clear structural link between the $HOC_6H_4C(O)R$ (R = H, *n*-alkyl) solid forms is the presence of a common $C_1^1(8)$ chain packing motif. The fact that no further structural trends are apparent in Table 3 highlights the difficulty in predicting polymorphism outcomes.

In most cases, only one molecule is present in the asymmetric unit. Exceptions occur for HAP(cr II), and the only known form of HBP, which have $Z' = 2$. It may at this stage be pointed out that, as previously noted,[8,36] no necessary correlation between the number of molecules in the asymmetric unit and the relative stability of polymorphs exists. Although it has been proposed that high Z' polymorphs should be metastable relative to their lower Z' counterparts,[73,74] the generality of this statement has been questioned,[8,36,75,76] based on cases such as the HAP system, where form II ($Z' = 2$) is more stable at 298 K than form I ($Z' = 1$).[8,36]

Table 3. Selected Structural and Energetic Data for All Known Crystal Forms of the $HOC_6H_4C(O)R$ (R = H, *n*-Alkyl) Family

R	compound (acronym)	form	Refcode	*T*/K	crystal system	space group	Z'/Z	ρ/g·cm^{-3}	E/Z[a]	$\Delta_{lat}H^o_m$/kJ·mol^{-1}[b]
H	4′-hydroxybenzaldehyde (HBA)	I[c]	PHBALD10	295	monoclinic	$P2_1/c$	1/4	1.358	*Z*	99.7 ± 0.4
		II[d]	PHBALD11	296	monoclinic	$P2_1/c$	1/4	1.357	*Z*	100.2 ± 2.8
CH_3	4′-hydroxyacetophenone (HAP)	I[e]	HACTPH13	298	monoclinic	$P2_1/c$	1/4	1.247	*E*	103.2 ± 0.8
		I[f]	HACTPH22	296	monoclinic	$P2_1/c$	1/4	1.267	*E*	
		II[e]	HACTPH15	298	orthorhombic	$P2_12_12_1$	2/8	1.278	*Z*	104.3 ± 0.4
		II[g]	HACTPH10	293	orthorhombic	$P2_12_12_1$	2/8	1.297	*Z*	
		II[f]	HACTPH19	300	orthorhombic	$P2_12_12_1$	2/8	1.271	*Z*	
C_3H_7	4′-hydroxybutyrophenone (HBP)	*h*	IDOSUQ	293	monoclinic	$P2_1/c$	2/8	1.206	*E*	116.7 ± 1.3
C_4H_9	4′-hydroxyvalerophenone (HVP)	I[i]	KERPUT	298	monoclinic	$P2_1/c$	1/4	1.202	*Z*	125.9 ± 0.6
		II	this work	296	monoclinic	$C2/c$	1/8	1.137	*E*	119.4 ± 1.1
		III	this work	222	monoclinic	$C2/c$	1/8	1.216	*E*	120.9 ± 1.1

[a]Molecular conformation. [b]Ref 44. [c]Ref 30. [d]Ref 35. [e]Ref 36. [f]Ref 37. [g]Ref 39. [h]Only one form has been reported, ref 32. [i]Ref 33.

https://dx.doi.org/10.1021/acs.cgd.9b01481
Cryst. Growth Des. 2020, 20, 2321−2336

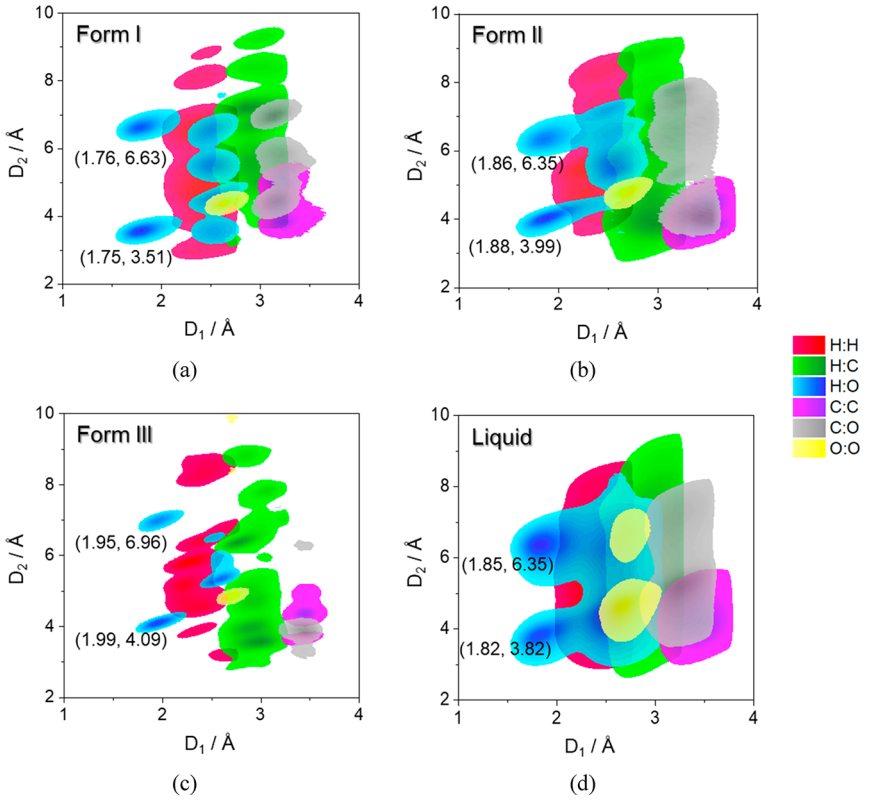

Figure 10. Results of a first shell analysis (FSA) on solid and liquid HVP: (a) form I at 298 K, (b) form II at 298 K, (c) form III at 150 K, and (d) liquid at 350 K. More intense colors correspond to higher probabilities. The values of D_1 and D_2 maxima are indicated as (D_1, D_2).

Conformational polymorphism is observed for forms I and II of HVP and HAP, but no link between the preference for a specific molecular conformation and the low or high temperature nature of a polymorph can be drawn. For example, the molecular conformation is *E* in the low temperature forms II and III of HVP and *Z* in the high temperature form I; in contrast, for HAP, the conformation in the low temperature form II is *Z* and *E* in the high temperature form I. There is also no relationship between molecular conformation and the monotropic or enantiotropic nature of a polymorphic pair: the HVP I/II forms are monotropic, whereas the HAP I/II are enantiotropic. It may also be noted that the II/III HVP and I/II HBA systems, where both polymorphs have a very similar packing and share an identical molecular conformation, are enantiotropic. This, however, does not represent a trend, since an enantiotropic relationship can also be observed in the case of the structurally dissimilar II/I HAP system. Furthermore, the structural similarity within an enantiotropic polymorphic pair does not imply that a reversible phase transition can be observed: for example, the III → II solid−solid transition in HVP is reversible but the I → II transition in HBA is not.

The observed density differences between polymorphs are <2.5%, except for HVP where differences of ∼7% are noted when form II is compared with the other two polymorphs. In energetic terms, Table 3 shows that, as previously reported,[44] the lattice enthalpy increases in an approximately linear way with the number of carbon atoms in the R group. It can also be noted that, as expected, for polymorphic pairs where density and lattice enthalpy data at ∼298 K exists, the denser form has the higher $\Delta_{lat}H^{o}_{m}$. In general, the lattice enthalpy differences between polymorphs in Table 3 are within 1 kJ·mol^{-1}, except for HVP where they reach ∼7 kJ·mol^{-1} when form I is compared with forms II and III.

Molecular Dynamics (MD) Simulations. MD simulations were performed to address two main questions: Why does the crystallization of HVP from the melt preferentially lead to the metastable form II and not to the more stable form I? How does form III transform into form II?

As a first step, the accuracy of the selected model was evaluated, by comparing the phase transition enthalpies and unit cell dimensions of the three HVP polymorphs obtained from the MD simulations, with the corresponding experimental values (see Tables S9 and S10 in the Supporting Information). The deviations of 1.2 kJ·mol^{-1} and 1.0 kJ·mol^{-1} found between the calculated, $\Delta_{trs}H^{o}_{m}$(III → II, 178 K) = 0.3 ± 0.7 kJ·mol^{-1} and $\Delta_{trs}H^{o}_{m}$(II → I, 298 K) = −7.4 ± 1.1 kJ·mol^{-1}, and experimental values, $\Delta_{trs}H^{o}_{m}$(III → II, 247.5 K) = 1.5 ± 0.2 kJ·mol^{-1} and $\Delta_{trs}H^{o}_{m}$(II → I, 298 K) = −6.4 ± 0.9 kJ·mol^{-1}, are considerably smaller than the expected accuracy of this type of force field models (typically 5 kJ·mol^{-1}).[64] The computations were also able to correctly capture the endothermic and exothermic nature of the III → II and II → I transitions, respectively, albeit with an uncertainty larger than the value in the case of the III → II process. It may be pointed out that the reliable prediction of the energetics of polymorphic phase transitions constitutes a particularly demanding test for force field models used in MD simulations, given the relatively small values of the thermodynamic quantities involved. This stresses the importance of providing reliable experimental benchmarks, such as the $\Delta_{trs}H^{o}_{m}$ determined here, for force field validation in energetic terms. As highlighted in a recent study,[77] energetic predictions based on force fields developed from structural data alone can exhibit significant errors, even when the processes of interest are

https://dx.doi.org/10.1021/acs.cgd.9b01481
Cryst. Growth Des. 2020, 20, 2321−2336

accompanied by much larger enthalpy changes than polymorphic phase transitions (e.g., cohesive energies of solids).

In the case of the unit cell dimensions, the maximum differences between experimental and calculated results were ≤3.2% for forms I and III, and ≤6% for form II. Errors of ∼4% are typical of this type of simulation, and slightly higher deviations, such as the ∼6% found for *a* and *c* unit cell dimensions of form II, are not uncommon.[64]

Why Does the Crystallization of HVP from the Melt Preferentially Lead to the Metastable Form II and Not to the More Stable Form I? Insights into this question were obtained by comparing the molecular organization patterns given by the simulations for liquid HVP at 350 K (∼15 K above the fusion temperature of form I), with those for polymorphs I and II at 298 K and form III at 150 K. The comparison was based on the computation of First Shell Analysis (FSA)[66] fingerprint plots and Combined Distribution Functions (CDF).

The FSA approach, as implemented in the program AGGREGATES,[66] produces two-dimensional plots resembling Hirshfeld surfaces.[78,79] The underlying methodology is, however, different and was specifically developed to investigate the molecular organization inside MD simulation boxes containing thousands of molecules in the solid or liquid states.[66] In brief, in a FSA study, the distance of each atom of every molecule in the simulation box to its closest neighbor in an adjacent molecule is determined. This distance is then taken as dimension D_1 for the construction of a 2D histogram. The second dimension, D_2, corresponds to the distance between the atom under consideration and the center of mass of the neighbor molecule. The program also allows the decomposition of the obtained pattern by types of atomic contacts (e.g., H:H, O:O, C:H, etc.).

The FSA fingerprint plots obtained for HVP in the solid (forms I, II and III) and liquid states are shown in Figure 10. This illustration clearly shows that the structure of the liquid is closer to form II than to forms I or III. The marked difference to form III is not unexpected, given that this phase is originated from form II and is only stable well below the temperature at which crystallization occurs. Furthermore, albeit the SCXRD results indicated similar packing patterns for forms II and III, they also revealed significant variations in molecular interaction distances and angles between the two forms, which necessarily influence their FSAs.

Two features are particularly significant when comparing liquid HVP with forms I and II: (i) the fact that the $OH_{hydroxyl}\cdots O$ hydrogen bond domains (blue domains in the range 1.5 Å < D_1 < 2.3 Å) in the liquid and in form II are centered at comparable positions; (ii) the distance between the maxima of the two $OH_{hydroxyl}\cdots O$ domains (ΔD_2) for the liquid state (ΔD_2 = 2.53 Å) is closer to that of form II (ΔD_2 = 2.36 Å) than that of form I (ΔD_2 = 3.12 Å). This suggests that a planar local organization of the molecules (analogous to that in form II) is most likely present in liquid HVP. Additional details of the FSA analysis are given as Supporting Information. It should also be pointed out that the reliability of the liquid structure used for comparison was tested, by confirming that the pattern in Figure 10d remained essentially unchanged when the simulations were started from boxes with different configurations (see Figure S7 in the Supporting Information). An identical conclusion was reached when this test was extended to the Combined Distribution Functions (CDF) analysis used to provide further insights into the structural similarity of liquid and form II HVP (see Figure S8 in the Supporting Information).

The CDF analysis was focused on the relationship between the angle defined by the aromatic ring planes, φ_{ring}, of any pair of molecules in the simulation box and the corresponding distance, $d_{C\cdots C}$, between the aromatic carbons linked to the −C(O)R group. As shown in Figure 11, the most probable angle for

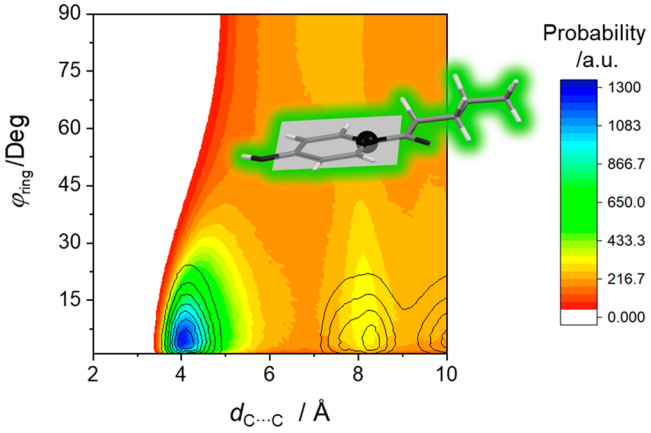

Figure 11. Comparison between the combined distribution functions (CDF) obtained for liquid (colored probability map) and form II (contour map) HVP, correlating the angle, φ_{ring}, defined by the aromatic ring planes of any two molecules in the simulation box and the corresponding distance, $d_{C\cdots C}$, between the aromatic carbons linked to the −C(O)R group (see molecule in the inset: aromatic ring plane in gray and reference aromatic carbon as a black sphere).

adjacent molecules in the liquid and in Form II is $\varphi_{ring} \approx 5°$. This is consistent with the propensity of the HVP molecules to adopt a planar stacking in the liquid state like that in form II. A closer affinity with form I would imply the observation of a significant probability of finding aromatic rings at ∼90° (see Figures 6 and S2), which is not corroborated by Figure 11. Note that, planarity should strictly correspond to $\varphi_{ring} \approx 0°$, as seen in the SCXRD results. Thus, the MD prediction that $\varphi_{ring} \approx 5°$, not only for liquid but also for form II HVP, probably reflects the limitations of the theoretical model to exactly capture fine aspects of the experimental observations. The existence of this discrepancy does not, however, invalidate the conclusion that the structure of liquid HVP is considerably more like form II than form I.

In conclusion, both the FSA and CDF analyses of the MD simulation results suggest that, when crystallization occurs from the melt, the HVP molecules tend to preserve the planar stacking organization present in the liquid phase. This leads to the preferential formation of the metastable form II, which exhibits this type of packing, rather than the thermodynamically stable form I, where a "herringbone" organization is present (Figure 6).

How Does Form III Transform to Form II? To investigate the molecular processes behind the III → II phase transition, observed by DSC at 247.5 ± 0.4 K, a simulation box consisting of 2 × 5 × 3 form III unit cells stacked along the three cell axes was first equilibrated at 150 K and then heated to 210 K at a rate of 10 K·ns^{-1}. The occurrence of the III → II conversion was signaled at ∼178 K by an abrupt and significant change in the geometry of the simulation box (Figures 12 and 13; see also Table S12 and video 3 given as Supporting Information): the *a* and *c* unit cell dimensions increased by 1.33 and 0.04 Å (2.66 and 0.11 Å, in terms of the box dimension along the *a* axis), respectively, *b* decreased by 0.44 Å (2.17 Å in terms of the box dimension along the *b* axis), *β* decreased by 1.7° (changing from 107.5° to 105.8°), and the density decreased by 0.042 g·cm^{-3}

https://dx.doi.org/10.1021/acs.cgd.9b01481
Cryst. Growth Des. 2020, 20, 2321−2336

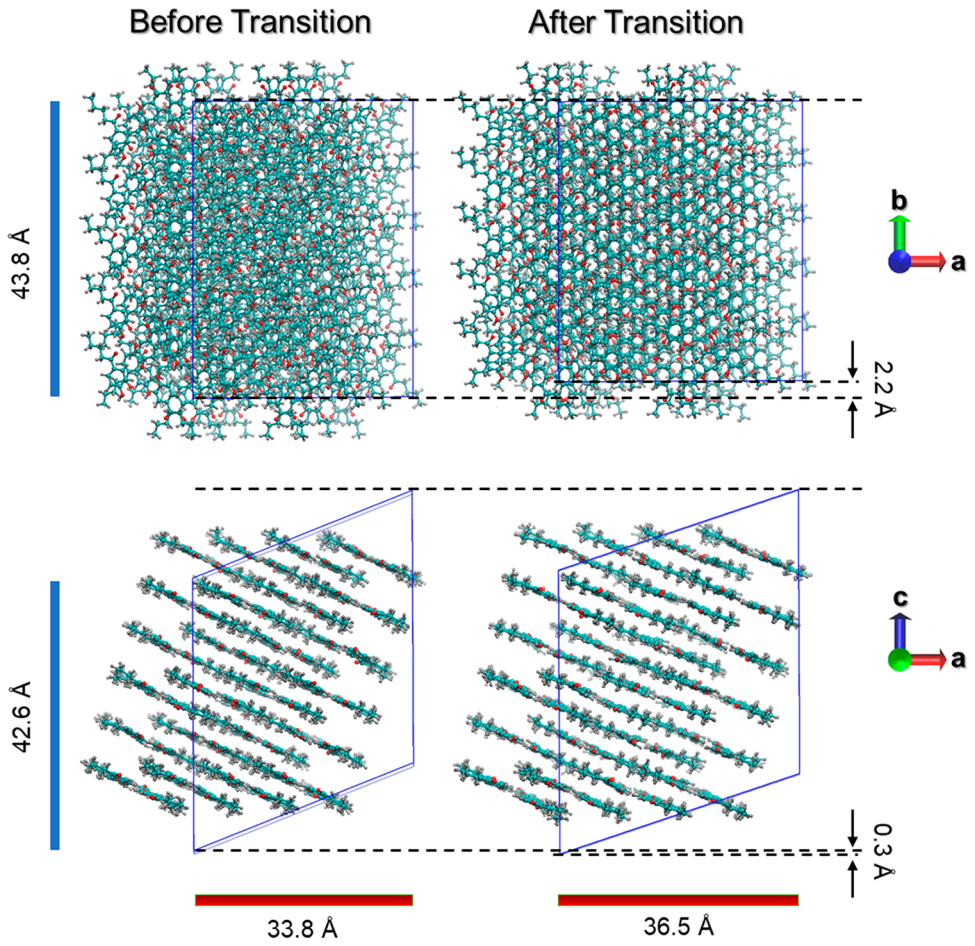

Figure 12. Snapshots of the MD simulation boxes before and after the HVP III → II phase transition, observed at 178 K.

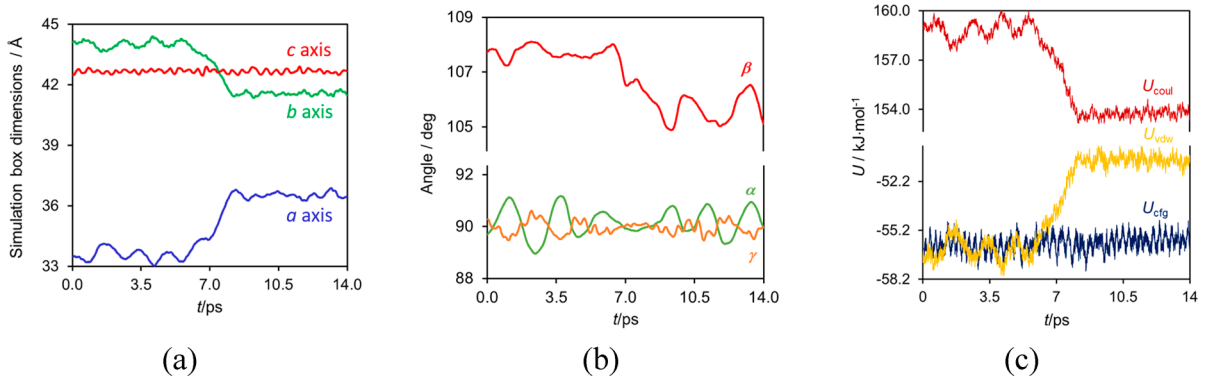

Figure 13. Changes in the simulation box dimensions (a), angles (b), and internal energy of the system (c) over time (t), during the III → II phase transition, at approximately 178 K. The origin of the time scale was arbitrarily set to ∼5 ps before the onset of the phase transition. U_{cfg} represents the internal configurational energy of the system; U_{vdw} and U_{coul} are the van der Waals and Coulomb contributions to U_{cfg}.

(1.179 g·cm^{-3} to 1.137 g·cm^{-3}). These variations are close to those noted in Table 1 when the experimental data for forms III (222 K) and II (296 K) are compared: a and c increase by 2.0 and 0.2 Å, respectively, b decreases by 0.53 Å, β increases by 0.41°, and the density decreases by 0.071 g·cm^{-3} (1.216 g·cm^{-3} to 1.145 g·cm^{-3}). It is noteworthy that, except for β, the model was able to correctly reproduce all the experimental trends in the variation of unit cell dimensions and density accompanying the III → II process.

The temperature of the phase transition predicted by the simulations is lower by ∼70 K than experimentally found by DSC. Shifts of this magnitude to lower temperatures have been previously observed in MD simulations of organic[80] and inorganic[81] compounds. It is nevertheless remarkable that the III → II phase transition could be evidenced by the present model, which was solely optimized to reproduce the experimental unit cell dimensions (Table 1) and the $\Delta_{trs}H^{o}_{m}$ values (Table S10) obtained in this work.

In addition, the MD simulations were also able to capture the changes in relative orientation of the molecules accompanying the III → II process noted in the SCXRD experiments (Figure 8). Indeed, the CDF results in Figure S9 (see Supporting

https://dx.doi.org/10.1021/acs.cgd.9b01481
Cryst. Growth Des. 2020, 20, 2321−2336

Information) show that (i) the angle between the alkyl chains (φ_{chain}) increases by ~12.4°, while the distance between the rings, measured as the distance between the aromatic carbons linked to the −C(O)R group ($d_{C\cdots C}$), increases by ~0.05 Å; (ii) the $O_{carbonyl}\cdots H-O_{hydroxyl}$ hydrogen bond angle ($\varphi_{H\text{-}bond}$) varies from ~158° to ~180°; and (iii) the corresponding $O_{carbonyl}\cdots O_{hydroxy}$ distance ($d_{O\cdots O}$) decreases by ~0.07 Å. This is in good agreement with the SCXRD results (Figure 8), indicating that φ_{chain} increases by 13°, $d_{C\cdots C}$ increases by ~0.3 Å, $\varphi_{H\text{-}bond}$ increases by 16.5°, and $d_{O\cdots O}$ decreases by 0.006 Å. Most notable, consistent with the experimental evidence, the III → II transformation was found to occur rapidly (2 ps, Figure 13), through an almost simultaneous movement of the HVP molecules in the entire simulation box, and without any evidence of a transition front propagation (see video 3 in the Supporting Information). These modifications lead to changes in the Coulomb and van der Waals contributions to the potential energy of the crystal (Figure 13), which, albeit significant, mutually cancel out to a large extent (see Table S11 of the Supporting Information). The Coulomb term becomes less repulsive by 5.1 ± 0.6 kJ·mol^{-1}, possibly because upon phase transition stronger H-bonds are formed (shorter distances and angle closer to 180° in form II than in form III). However, such an advantage is offset by the van der Waals contribution becoming less negative by 5.5 ± 0.7 kJ·mol^{-1}. This may be originated by the less efficient packing of the HVP molecules in form II (the packing index and density decrease by 5−6% relative to form III, Table 1) accompanied by an increase of the separation between the alkyl chains and the aromatic rings (Figure 8). The difference $U_{vdw} - U_{coul}$ essentially accounts for most of the change in configurational energy associated with the phase transition, which was found to be $U^{o}_{cfg,\,m}(III) - U^{o}_{cfg,\,m}(II)$ = 0.3 ± 0.7 kJ·mol^{-1}. This results from the fact that the intramolecular and long-range correction contributions for the internal energy of the crystal are essentially identical before and after the transition and, therefore, cancel out (see Table S11 of the Supporting Information). Since the internal energy to enthalpy correction is approximately the same for the two polymorphs, it is possible to assume that $\Delta_{trs}H^{o}_{m}(III \rightarrow II) \approx U^{o}_{cfg,\,m}(II) - U^{o}_{cfg,\,m}(III)$ = 0.3 ± 0.7 kJ·mol^{-1}. Albeit supported by a small value (~0.3 kJ·mol^{-1}) with a relatively large uncertainty, the conclusion that the III → II transition is endothermic, hence the lattice enthalpy is smaller for form II than for form III, is in agreement with $\Delta_{trs}H^{o}_{m}(III \rightarrow II)$ = 1.5 ± 0.2 kJ·mol^{-1} experimentally obtained by DSC. It is also corroborated by the experimentally found $\Delta_{lat}H^{o}_{m}$(cr II) = 119.4 ± 1.1 kJ·mol^{-1} and $\Delta_{lat}H^{o}_{m}$(cr III) = 120.9 ± 1.1 kJ·mol^{-1}. Thus, both MD and experimental evidence suggest that the III → II phase transition is entropically driven. The fact that according to the simulations the endothermicity of the III → II process is linked to the dominance of van der Waals over Coulomb contributions highlights the importance of the former type of interactions in the stabilization of polymorphs.

As mentioned above, the III → II phase transition is accompanied by a decrease in density and packing index (Table 1). It seems, therefore, reasonable to assume that the entropic gain driving the process, results, at least in part, from an increase in conformational freedom of the HVP molecules. This hypothesis was tested by analyzing the distribution of the alkyl chain dihedral angle, $\varphi_{c\text{-}c\text{-}c\text{-}c}$, at a series of temperatures above and below the phase transition (Figure 14). The obtained results indicate that, indeed, before the phase transition (T < 170 K) the alkyl chains adopt a narrow range of conformations centered at

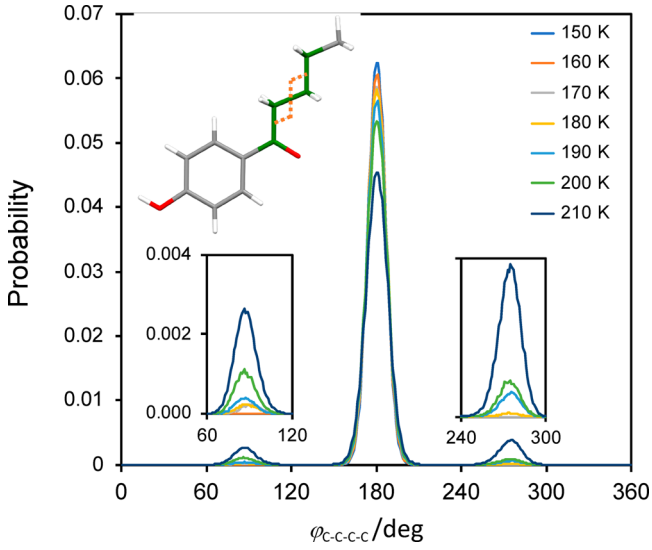

Figure 14. Distribution of the alkyl chain dihedral angle $\varphi_{C-C-C-C}$ (in orange, see molecule in the inset) as a function of temperature, obtained from MD simulations.

$\varphi_{c\text{-}c\text{-}c\text{-}c}$ = 180°. After the phase transition, the conformational diversity progressively increases, and at 210 K ca. 12% of the molecules have $\varphi_{c\text{-}c\text{-}c\text{-}c}$ at 90° or 270°.

CONCLUSIONS

The structures of two new polymorphs of 4′-hydroxyvalerophenone (forms II and III) have been determined by single crystal X-ray diffraction (SCXRD). Forms II and III are very similar in terms of molecular conformation and packing. They share with the previously known form I the presence of a $C_1^1(8)$ infinite chain sustained by "head-to-tail" OH···O hydrogen bonds as the main 1D packing motif. However, they significantly differ from form I in both the molecular organization within the chain (herringbone in form I; planar in forms II and III) and the conformation of the HVP molecule (the configuration of the CO and OH groups is *Z* in form I and *E* in forms II and III).

These structural differences are reflected by the thermodynamics and kinetics of the III → II and II → I transitions. SCXRD, DSC, and microscopy experiments showed that the structurally similar forms III and II are enantiotropically related by a fast and reversible phase transition (T_{trs} = 247.5 ± 0.4 K), that can occur under single crystal to single crystal conditions. In contrast, the II → I transition, which involves a considerable packing rearrangement accompanied by a change in molecular conformation, is severely hindered, albeit form II is less stable than form I up to fusion (i.e., the two forms are monotropically related). In fact, form II can be melted, or stored for days at ambient temperature and pressure, without signs of transformation into form I, unless subject to a perturbation such as gentle grinding.

In line with these conclusions, both the microscopy observations and MD simulations suggested that the III → II transition is likely to occur by a mechanism involving a concerted movement of the molecules in the lattice, while the II → I conversion follows a diffusive nucleation and growth process.

MD simulations further indicated that the structure of liquid HVP is closer to form II than to form I. The preference of HVP to crystallize from the melt as the metastable form II rather than

https://dx.doi.org/10.1021/acs.cgd.9b01481
Cryst. Growth Des. 2020, 20, 2321−2336

the stable form I (in accordance with Ostwald's rule of stages), should, therefore, be due to this structural similarity.

A thermodynamic analysis based on the Gibbs energies of the III → I and II → I transitions suggested that the relative stability of the three polymorphs at 298 K follows the order I > II > III, which is distinct from the corresponding lattice enthalpy ranking I > III > II. This stresses the fact that $\Delta_{lat}H^{o}_{m}$ is not necessarily a reliable indicator of polymorph stability, because entropic factors can also play a determinant role.

Finally, the combined thermodynamic, SCXRD, and MD results indicated that the presence of stronger classical hydrogen bonds in a polymorph (OH···O in the present work) may not be synonymous of a larger lattice enthalpy. Indeed, although such correlation is found when the I/II pair is considered, the same is not true for the II/III forms. Here, the relationship $\Delta_{lat}H^{o}_{m}$(cr II) < $\Delta_{lat}H^{o}_{m}$(cr III) is observed, despite the fact that stronger H-bonds are likely to be present in form II than in form III. This highlights the importance of van der Waals contributions, since according to MD evidence, they are responsible for the lattice enthalpy inversion in the case of polymorphs II and III.

■ ASSOCIATED CONTENT

Supporting Information

The Supporting Information is available free of charge at https://pubs.acs.org/doi/10.1021/acs.cgd.9b01481.

Figure S1 with an overlay of the molecular structures of HVP forms I and III at different temperatures. Figure S2 showing the local organization of the HVP molecules in the single crystal X-ray diffraction structure of form I, at 298 K. Detailed results of the enthalpy of transition (Tables S1−S5) and heat capacity (Tables S6 and S7) measurements by DSC. Details of the calculation of enthalpies, entropies, and Gibbs energies in Table 2 and assignment of uncertainties to thermodynamic data. Details of the MD simulations including force field parametrization and results (Figures S3−S9 and Tables S8−S12) (PDF)

Videos 1−3 with the microscopy and MD simulation results for the III → II and II → I phase transitions (MP4-1, MP4-2, and MP4-3)

Accession Codes

CCDC 1961728−1961731 contain the supplementary crystallographic data for this paper. These data can be obtained free of charge via www.ccdc.cam.ac.uk/data_request/cif, or by emailing data_request@ccdc.cam.ac.uk, or by contacting The Cambridge Crystallographic Data Centre, 12 Union Road, Cambridge CB2 1EZ, UK; fax: +44 1223 336033.

■ AUTHOR INFORMATION

Corresponding Author

Manuel E. Minas da Piedade − *Centro de Química Estrutural, Faculdade de Ciências Universidade de Lisboa, 1749-016 Lisboa, Portugal;* orcid.org/0000-0001-7550-6952; Phone: +351-21-7500866; Email: memp@fc.ul.pt; Fax: +351-21-7500088

Authors

Ricardo G. Simões − *Centro de Química Estrutural, Faculdade de Ciências Universidade de Lisboa, 1749-016 Lisboa, Portugal;* orcid.org/0000-0003-4989-4087

Cátia S. D. Lopes − *Centro de Química Estrutural, Faculdade de Ciências Universidade de Lisboa, 1749-016 Lisboa, Portugal*

M. Fátima M. Piedade − *Centro de Química Estrutural, Faculdade de Ciências Universidade de Lisboa, 1749-016 Lisboa, Portugal; Centro de Química Estrutural, Instituto Superior Técnico, Universidade de Lisboa, 1049-001 Lisboa, Portugal*

Carlos E. S. Bernardes − *Centro de Química Estrutural, Faculdade de Ciências Universidade de Lisboa, 1749-016 Lisboa, Portugal;* orcid.org/0000-0003-1490-9728

Hermínio P. Diogo − *Centro de Química Estrutural, Instituto Superior Técnico, Universidade de Lisboa, 1049-001 Lisboa, Portugal;* orcid.org/0000-0002-0808-1306

Complete contact information is available at: https://pubs.acs.org/10.1021/acs.cgd.9b01481

Notes

The authors declare no competing financial interest.

■ ACKNOWLEDGMENTS

This work was supported by Fundação para a Ciência e a Tecnologia (FCT), Portugal through Projects PTDC/QUI-OUT/28401/2017 (LISBOA-01-0145-FEDER-028401), UIDB/00100/2020, and UIDP/00100/2020. Postdoctoral and doctoral grants awarded by FCT to R.G.S. (SFRH/BPD/118771/2016), and C.S.D.L. (SFRH/BD/128794/2017), respectively, are also gratefully acknowledged.

■ DEDICATION

This article is dedicated to the memory of Professor Joel Bernstein who, at a meeting that took place just a few months before passing away, was still strongly encouraging us to pursue this holistic way of looking at polymorphism.

■ REFERENCES

(1) Bernstein, J. *Polymorphism in Molecular Crystals*; Oxford University Press: New York, 2002.

(2) Brittain, H. G. *Polymorphism in Pharmaceutical Solids*; Marcel Dekker: New York, 1999.

(3) Brittain, H. G. *Polymorphism in Pharmaceutical Solids*, 2nd ed.; Informa Healthcare: New York, 2009.

(4) Hilfiker, R. *Polymorphism in the Pharmaceutical Industry*; Wiley-VCH Verlag GmbH & Co.: Weinheim, 2006.

(5) Cruz-Cabeza, A. J.; Reutzel-Edens, S. M.; Bernstein, J. Facts and Fictions about Polymorphism. *Chem. Soc. Rev.* **2015**, *44*, 8619−8635.

(6) Davey, R. J.; Schroeder, S. L. M.; ter Horst, J. H. Nucleation of Organic Crystals - A Molecular Perspective. *Angew. Chem., Int. Ed.* **2013**, *52*, 2166−2179.

(7) Mullin, J. W. *Crystallization*; 4th ed.; Butterworth-Heinemann: Oxford, 2001.

(8) Joseph, A.; Bernardes, C. E. S.; Druzhinina, A. I.; Varushchenko, R. M.; Nguyen, T. Y.; Emmerling, F.; Yuan, L.; Dupray, V.; Coquerel, G.; Minas da Piedade, M. E. Polymorphic Phase Transition in 4′-Hydroxyacetophenone: Equilibrium Temperature, Kinetic Barrier, and the Relative Stability of Z' = 1 and Z' = 2 Forms. *Cryst. Growth Des.* **2017**, *17*, 1918−1932.

(9) Brandel, C.; Cartigny, Y.; Couvrat, N.; Eusébio, M. E. S.; Canotilho, J.; Petit, S.; Coquerel, G. Mechanisms of Reversible Phase Transitions in Molecular Crystals: Case of Ciclopirox. *Chem. Mater.* **2015**, *27*, 6360−6373.

(10) Mnyukh, Y. *Fundamentals of Solid-State Phase Transitions, Ferromagnetism and Ferroelectricity*; First Book Library: Milton Keynes, 2001.

(11) Lee, A. Y.; Erdemir, D.; Myerson, A. S. Crystal Polymorphism in Chemical Process Development. *Annu. Rev. Chem. Biomol. Eng.* **2011**, *2*, 259−280.

(12) Groom, C. R.; Bruno, I. J.; Lightfoot, M. P.; Ward, S. C. The Cambridge Structural Database. *Acta Crystallogr., Sect. B: Struct. Sci., Cryst. Eng. Mater.* **2016**, *B72*, 171−179.
(13) Westrum, E. F., Jr.; McCullough, J. P. Thermodynamics of Crystals; In *Physics and Chemistry of the Organic Solid State*; Fox, D.; Labes, M. M.; Weissberger, A., Eds.; Interscience: New York, 1963; Vol. *I*.
(14) Giron, D. Thermal Analysis and Calorimetric Methods in the Characterization of Polymorphs and Solvates. *Thermochim. Acta* **1995**, *248*, 1−59.
(15) Price, S. L. Computed Crystal Energy Landscapes for Understanding and Predicting Organic Crystal Structures and Polymorphism. *Acc. Chem. Res.* **2009**, *42*, 117−126.
(16) Cruz-Cabeza, A. J. Crystal Structure Prediction: Are We There Yet? *Acta Crystallogr., Sect. B: Struct. Sci., Cryst. Eng. Mater.* **2016**, *B72*, 437−438.
(17) Reilly, A. M.; Cooper, R. I.; Adjiman, C. S.; Bhattacharya, S.; Boese, A. D.; Brandenburg, J. G.; Bygrave, P. J.; Bylsma, R.; Campbell, J. E.; Car, R.; Case, D. H.; Chadha, R.; Cole, J. C.; Cosburn, K.; Cuppen, H. M.; Curtis, F.; Day, G. M.; DiStasio, R. A.; Dzyabchenko, A.; van Eijck, B. P.; Elking, D. M.; van den Ende, J. A.; Facelli, J. C.; Ferraro, M. B.; Fusti-Molnar, L.; Gatsiou, C. A.; Gee, T. S.; de Gelder, R.; Ghiringhelli, L. M.; Goto, H.; Grimme, S.; Guo, R.; Hofmann, D. W. M.; Hoja, J.; Hylton, R. K.; Iuzzolino, L.; Jankiewicz, W.; de Jong, D. T.; Kendrick, J.; de Klerk, N. J. J.; Ko, H. Y.; Kuleshova, L. N.; Li, X. Y.; Lohani, S.; Leusen, F. J. J.; Lund, A. M.; Lv, J.; Ma, Y. M.; Marom, N.; Masunov, A. E.; McCabe, P.; McMahon, D. P.; Meekes, H.; Metz, M. P.; Misquitta, A. J.; Mohamed, S.; Monserrat, B.; Needs, R. J.; Neumann, M. A.; Nyman, J.; Obata, S.; Oberhofer, H.; Oganov, A. R.; Orendt, A. M.; Pagola, G. I.; Pantelides, C. C.; Pickard, C. J.; Podeszwa, R.; Price, L. S.; Price, S. L.; Pulido, A.; Read, M. G.; Reuter, K.; Schneider, E.; Schober, C.; Shields, G. P.; Singh, P.; Sugden, I. J.; Szalewicz, K.; Taylor, C. R.; Tkatchenko, A.; Tuckerman, M. E.; Vacarro, F.; Vasileiadis, M.; Vazquez-Mayagoitia, A.; Vogt, L.; Wang, Y. C.; Watson, R. E.; de Wijs, G. A.; Yang, J.; Zhu, Q.; Groom, C. R. Report on the Sixth Blind Test of Organic Crystal Structure Prediction Methods. *Acta Crystallogr., Sect. B: Struct. Sci., Cryst. Eng. Mater.* **2016**, *72*, 439−459.
(18) Adjiman, C. S.; Brandenburg, J. G.; Braun, D. E.; Cole, J.; Collins, C.; Cooper, A. I.; Cruz-Cabeza, A. J.; Day, G. M.; Dudek, M.; Hare, A.; Iuzzolino, L.; McKay, D.; Mitchell, J. B. O.; Mohamed, S.; Neelamraju, S.; Neumann, M.; Nilsson Lill, S.; Nyman, J.; Oganov, A. R.; Price, S. L.; Pulido, A.; Reutzel-Edens, S.; Rietveld, I.; Ruggiero, M. T.; Schon, J. C.; Tsuzuki, S.; van den Ende, J.; Woollam, G.; Zhu, Q. Applications of Cystal Structure Prediction - Organic Molecular Structures: General Discussion. *Faraday Discuss.* **2018**, *211*, 493−539.
(19) Nyman, J.; Reutzel-Edens, S. M. Crystal Structure Prediction is Changing from Basic Science to Applied Technology. *Faraday Discuss.* **2018**, *211*, 459−476.
(20) Price, S. L. Control and Prediction of the Organic Solid State: A Challenge to Theory and Experiment. *Proc. R. Soc. London, Ser. A* **2018**, *474*, 20180351.
(21) Anwar, J.; Zahn, D. Polymorphic Phase Transitions: Macroscopic Theory and Molecular Simulation. *Adv. Drug Delivery Rev.* **2017**, *117*, 47−70.
(22) Peng, Y.; Li, W.; Wang, F.; Still, T.; Yodh, A. G.; Han, Y. L. Diffusive and Martensitic Nucleation Kinetics in Solid-solid Transitions of Colloidal Crystals. *Nat. Commun.* **2017**, *8*, 14978.
(23) Peng, Y.; Wang, F.; Wang, Z. R.; Alsayed, A. M.; Zhang, Z. X.; Yodh, A. G.; Han, Y. L. Two-step Nucleation Mechanism in Solid-solid Phase Transitions. *Nat. Mater.* **2015**, *14*, 101−108.
(24) Nakamura, E. Atomic-Resolution Transmission Electron Microscopic Movies for Study of Organic Molecules, Assemblies, and Reactions: The First 10 Years of Development. *Acc. Chem. Res.* **2017**, *50*, 1281−1292.
(25) Zahn, D.; Anwar, J. Collective Displacements in a Molecular Crystal Polymorphic Transformation. *RSC Adv.* **2013**, *3*, 12810−12815.
(26) Braun, D. E.; Kruger, H.; Kahlenberg, V.; Griesser, U. J. Molecular Level Understanding of the Reversible Phase Transformation between Forms III and II of Dapsone. *Cryst. Growth Des.* **2017**, *17*, 5054−5060.
(27) Dunitz, J. D. Phase-Transitions in Molecular-Crystals from a Chemical Viewpoint. *Pure Appl. Chem.* **1991**, *63*, 177−185.
(28) Herbstein, F. H. Some Applications of Thermodynamics in Crystal Chemistry. *J. Mol. Struct.* **1996**, *374*, 111−128.
(29) van den Ende, J. A.; Ensing, B.; Cuppen, H. M. Energy Barriers and Mechanisms in Solid-solid Polymorphic Transitions Exhibiting Cooperative Motion. *CrystEngComm* **2016**, *18*, 4420−4430.
(30) Iwasaki, F. A Refinement of *p*-Hydroxybenzaldehyde. *Acta Crystallogr., Sect. B: Struct. Crystallogr. Cryst. Chem.* **1977**, *B33*, 1646−1648.
(31) Chenthamarai, S.; Jayaraman, D.; Meera, K.; Santhanaraghavan, P.; Subramanian, C.; Bocelli, G.; Ramasamy, P. Growth and Single Crystal XRD Characterization of Undoped and Doped 4-Hydroxyacetophenone. *Cryst. Eng.* **2001**, *4*, 37−48.
(32) Xu, B.; Feng, Z. Q.; Wang, J. T.; Hu, L. G.; Huang, J. 1-(4-Hydroxyphenyl) butan-1-one. *Acta Crystallogr., Sect. E: Struct. Rep. Online* **2006**, *62*, O2603−O2605.
(33) Luo, Z. H.; Zhu, H. J.; Liu, S. 1-(4-Hydroxyphenyl)pentan-1-one. *Acta Crystallogr., Sect. E: Struct. Rep. Online* **2006**, *62*, O5054−O5055.
(34) Simões, R. G.; Bernardes, C. E. S.; Minas da Piedade, M. E. Polymorphism in 4-Hydroxybenzaldehyde: A Crystal Packing and Thermodynamic Study. *Cryst. Growth Des.* **2013**, *13*, 2803−2814.
(35) Jasinski, J. P.; Butcher, R. J.; Narayana, B.; Swamy, M. T.; Yathirajan, H. S. Redetermination of 4-Hydroxybenzaldehyde. *Acta Crystallogr., Sect. E: Struct. Rep. Online* **2008**, *64*, No. o187.
(36) Bernardes, C. E. S.; Piedade, M. F. M.; Minas da Piedade, M. E. Polymorphism in 4′-Hydroxyacetophenone: Structure and Energetics. *Cryst. Growth Des.* **2008**, *8*, 2419−2430.
(37) Sztylko, M.; Malinska, M.; Petricek, V.; Gutmann, M. J.; Hoser, A. A. How Accurate do X-ray Data Need to be to Obtain a Reliable Order of Stability for Polymorphs? The Case Study of p-Hydroxyacetophenone Polymorphs. *Cryst. Growth Des.* **2019**, *19*, 5132−5141.
(38) Kresge, A. J.; Lough, A. J.; Zhu, Y. A Redetermination of 4′-Hydroxyacetophenone. *Acta Crystallogr., Sect. E: Struct. Rep. Online* **2002**, *58*, o1057−o1059.
(39) Vainshtein, B. K.; Lobanova, G. M.; Gurskaya, G. V. Crystal and Molecular Structure of *n*-Oxyacetophenone. *Kristallografiya* **1974**, *19*, 531−538.
(40) Bernardes, C. E. S.; Minas da Piedade, M. E. Crystallization of 4′-Hydroxyacetophenone from Water: Control of Polymorphism via Phase Diagram Studies. *Cryst. Growth Des.* **2012**, *12*, 2932−2941.
(41) Bernardes, C. E. S.; Piedade, M. F. M.; Minas da Piedade, M. E. Structure and Energetics of a New Hydrate of 4 ‘-Hydroxyacetophenone. *Cryst. Growth Des.* **2010**, *10*, 3070−3076.
(42) Bernardes, C. E. S.; Matos Lopes, M. L. S.; Ascenso, J. R.; Minas da Piedade, M. E. From Molecules to Crystals: The Solvent Plays an Active Role Throughout the Nucleation Pathway of Molecular Organic Crystals. *Cryst. Growth Des.* **2014**, *14*, 5436−5441.
(43) Lopes, C. S. D.; Bernardes, C. E. S.; Piedade, M. F. M.; Diogo, H. P.; Minas da Piedade, M. E. A New Polymorph of 4′-Hydroxyvalerophenone Revealed by Thermoanalytical and X-ray Diffraction Studies. *Eur. Phys. J.: Spec. Top.* **2017**, *226*, 849−855.
(44) Lopes, C. S. D.; Agapito, F.; Bernardes, C. E. S.; Minas da Piedade, M. E. Thermochemistry of 4-HOC$_6$H$_4$COR (R = H, CH$_3$, C$_2$H$_5$, *n*-C$_3$H$_7$, *n*-C$_4$H$_9$, *n*-C$_5$H$_{11}$, and *n*-C$_6$H$_{13}$) Compounds. *J. Chem. Thermodyn.* **2017**, *104*, 281−287.
(45) *SABADS, Area-detector Absorption Correction*; Bruker AXS Inc.: Madison, WI, 2004.
(46) *SAINT, Area-detector Integration Software*, Version7.23; Bruker AXS Inc.: Madison, WI, 2004.
(47) Sheldrick, G. M. A Short History of SHELX. *Acta Crystallogr., Sect. A: Found. Crystallogr.* **2008**, *A64*, 112−122.
(48) Farrugia, L. J. WinGX and ORTEP for Windows: An Update. *J. Appl. Crystallogr.* **2012**, *45*, 849−854.

https://dx.doi.org/10.1021/acs.cgd.9b01481
Cryst. Growth Des. 2020, 20, 2321−2336

(49) Macrae, C. F.; Edgington, P. R.; McCabe, P.; Pidcock, E.; Shields, G. P.; Taylor, R.; Towler, M.; van de Streek, J. Mercury: Visualization and Analysis of Crystal Structures. *J. Appl. Crystallogr.* **2006**, *39*, 453−457.
(50) Spek, A. L. Structure Validation in Chemical Crystallography. *Acta Crystallogr., Sect. D: Biol. Crystallogr.* **2009**, *D65*, 148−155.
(51) Martinho Simões, J. A.; Minas da Piedade, M. E. *Molecular Energetics Condensed Phase Thermochemical Techniques*; Oxford University Press: New York, 2008.
(52) Joseph, A.; Bernardes, C. E. S.; Minas da Piedade, M. E. Heat Capacity and Thermodynamics of Solid and Liquid Pyridine-3-carboxylic Acid (Nicotinic acid) Over the Temperature Range 296 to 531 K. *J. Chem. Thermodyn.* **2012**, *55*, 23−28.
(53) Bernardes, C. E. S. CB-MScope 01 - A Program for Microscope Control and Data Acquisition; FCUL: Lisbon, 2019.
(54) Plimpton, S. Fast Parallel Algorithms for Short-Range Molecular-Dynamics. *J. Comput. Phys.* **1995**, *117*, 1−19.
(55) Abraham, M. J.; Murtola, T.; Schulz, R.; Pall, S.; Smith, J. C.; Hess, B.; Lindahl, E. GROMACS: High Performance Molecular Simulations Through Multi-level Parallelism from Laptops to Supercomputers. *SoftwareX* **2015**, *1−2*, 19−25.
(56) Jorgensen, W. L.; Maxwell, D. S.; Tirado-Rives, J. Development and Testing of the OPLS All-Atom Force Field on Conformational Energetics and Properties of Organic Liquids. *J. Am. Chem. Soc.* **1996**, *118*, 11225−11236.
(57) Kaminski, G.; Jorgensen, W. L. Performance of the AMBER94, MMFF94, and OPLS-AA Force Fields for Modeling Organic Liquids. *J. Phys. Chem.* **1996**, *100*, 18010−18013.
(58) Breneman, C. M.; Wiberg, K. B. Determining Atom-Centered Monopoles from Molecular Electrostatic Potentials. The Need for High Sampling Density in Formamide Conformational Analysis. *J. Comput. Chem.* **1990**, *11*, 361−373.
(59) Frisch, M. J.; Head-Gordon, M.; Pople, J. A. A Direct MP2 Gradient Method. *Chem. Phys. Lett.* **1990**, *166*, 275−280.
(60) Frisch, M. J.; Head-Gordon, M.; Pople, J. A. Semi-Direct Algorithms for the MP2 Energy and Gradient. *Chem. Phys. Lett.* **1990**, *166*, 281−289.
(61) Head-Gordon, M.; Head-Gordon, T. Analytic MP2 Frequencies without Fifth-Order Storage. Theory and Application to Bifurcated Hydrogen-Bonds in the Water Hexamer. *Chem. Phys. Lett.* **1994**, *220*, 122−128.
(62) Head-Gordon, M.; Pople, J. A.; Frisch, M. J. MP2 Energy Evaluation by Direct Methods. *Chem. Phys. Lett.* **1988**, *153*, 503−506.
(63) Woon, D. E.; Dunning, T. H. Gaussian-Basis Sets for Use in Correlated Molecular Calculations. III The Atoms Aluminum through Argon. *J. Chem. Phys.* **1993**, *98*, 1358−1371.
(64) Bernardes, C. E. S.; Joseph, A. Evaluation of the OPLS-AA Force Field for the Study of Structural and Energetic Aspects of Molecular Organic Crystals. *J. Phys. Chem. A* **2015**, *119*, 3023−3034.
(65) Simões, R. G.; Bernardes, C. E. S.; Diogo, H. P.; Agapito, F.; Minas da Piedade, M. E. Energetics of Simvastatin. *Mol. Pharmaceutics* **2013**, *10*, 2713−2722.
(66) Bernardes, C. E. S. AGGREGATES: Finding Structures in Simulation Results of Solutions. *J. Comput. Chem.* **2017**, *38*, 753−765.
(67) Humphrey, W.; Dalke, A.; Schulten, K. VMD: Visual Molecular Dynamics. *J. Mol. Graphics* **1996**, *14*, 33−38.
(68) Frisch, M. J.; Trucks, G. W.; Schlegel, H. B.; Scuseria, G. E.; Robb, M. A.; Cheeseman, J. R.; Scalmani, G.; Barone, V.; Mennucci, B.; Petersson, G. A.; Nakatsuji, H.; Caricato, M.; Li, X.; Hratchian, H. P.; Izmaylov, A. F.; Bloino, J.; Zheng, G.; Sonnenberg, J. L.; Hada, M.; Ehara, M.; Toyota, K.; Fukuda, R.; Hasegawa, J.; Ishida, M.; Nakajima, T.; Honda, Y.; Kitao, O.; Nakai, H.; Vreven, T.; Montgomery, J. A., Jr.; Peralta, J. E.; Ogliaro, F.; Bearpark, M. J.; Heyd, J.; Brothers, E. N.; Kudin, K. N.; Staroverov, V. N.; Kobayashi, R.; Normand, J.; Raghavachari, K.; Rendell, A. P.; Burant, J. C.; Iyengar, S. S.; Tomasi, J.; Cossi, M.; Rega, N.; Millam, N. J.; Klene, M.; Knox, J. E.; Cross, J. B.; Bakken, V.; Adamo, C.; Jaramillo, J.; Gomperts, R.; Stratmann, R. E.; Yazyev, O.; Austin, A. J.; Cammi, R.; Pomelli, C.; Ochterski, J. W.; Martin, R. L.; Morokuma, K.; Zakrzewski, V. G.; Voth, G. A.; Salvador, P.; Dannenberg, J. J.; Dapprich, S.; Daniels, A. D.; Farkas, Ö.; Foresman, J. B.; Ortiz, J. V.; Cioslowski, J.; Fox, D. J. *Gaussian 09 D.01*; Gaussian, Inc.: Wallingford, CT, USA, 2009.
(69) Burger, A.; Ramberger, R. Polymorphism of Pharmaceuticals and Other Molecular-Crystals. 1. Theory of Thermodynamic Rules. *Microchim. Acta* **1979**, *72*, 259−271.
(70) Dybeck, E. C.; Abraham, N. S.; Schieber, N. P.; Shirts, M. R. Capturing Entropic Contributions to Temperature-Mediated Polymorphic Transformations Through Molecular Modeling. *Cryst. Growth Des.* **2017**, *17*, 1775−1787.
(71) Piaggi, P. M.; Parrinello, M. Predicting Polymorphism in Molecular Crystals Using Orientational Entropy. *Proc. Natl. Acad. Sci. U. S. A.* **2018**, *115*, 10251−10256.
(72) Nyman, J.; Day, G. M. Static and Lattice Vibrational Energy Differences Between Polymorphs. *CrystEngComm* **2015**, *17*, 5154−5165.
(73) Das, D.; Banerjee, R.; Mondal, R.; Howard, J. A. K.; Boese, R.; Desiraju, G. R. Synthon Evolution and Unit Cell Evolution During Crystallisation. A Study of Symmetry-independent Molecules ($Z' > 1$) in Crystals of Some Hydroxy Compounds. *Chem. Commun.* **2006**, 555−557.
(74) Desiraju, G. R. On the Presence of Multiple Molecules in the Crystal Asymmetric Unit ($Z' > 1$). *CrystEngComm* **2007**, *9*, 91−92.
(75) Anderson, K. M.; Steed, J. W. Comment on "On the Presence of Multiple Molecules in the Crystal Asymmetric Unit ($Z' > 1$)" by Gautam R. Desiraju, CrystEngComm, 2007, 9, 91. *CrystEngComm* **2007**, *9*, 328−330.
(76) Nichol, G. S.; Clegg, W. Further Thoughts on Crystal Structures with ($Z' > 1$) Analysis of Single-crystal Structures Determined Using X-ray Synchrotron and Neutron Radiation in the Cambridge Structural Database. *CrystEngComm* **2007**, *9*, 959−960.
(77) Bernardes, C. E. S.; Donato, M. T.; Piedade, M. F. M.; Diogo, H. P.; Canongia Lopes, J. N.; Minas da Piedade, M. E. A Force Field for MD Simulations on Rhenium Organometallic Compounds Developed from Enthalpy of Sublimation and X-ray Diffraction Measurements. *J. Chem. Thermodyn.* **2019**, *133*, 60−69.
(78) Spackman, M. A. Molecules in Crystals. *Phys. Scr.* **2013**, *87*, 048103.
(79) Spackman, M. A.; Jayatilaka, D. Hirshfeld Surface Analysis. *CrystEngComm* **2009**, *11*, 19−32.
(80) Simões, R. G.; Bernardes, C. E. S.; Joseph, A.; Piedade, M. F. M.; Kraus, W.; Emmerling, F.; Diogo, H. P.; Minas da Piedade, M. E. Polymorphism in Simvastatin: Twinning, Disorder and Enantiotropic Phase Transitions. *Mol. Pharmaceutics* **2018**, *15*, 5349−5360.
(81) Abascal, J. L. F.; Vega, C. A General Purpose Model for the Condensed Phases of Water: TIP4P/2005. *J. Chem. Phys.* **2005**, *123*, 234505.

https://dx.doi.org/10.1021/acs.cgd.9b01481
Cryst. Growth Des. 2020, 20, 2321−2336